Universidade de São Paulo
Instituto de Física

Vínculos Cosmológicos com o Auxílio do Efeito Sachs-Wolfe Integrado

Arthur Diniz Meirelles

Orientador: Prof. Dr. Edivaldo Moura Santos
Coorientador: Prof. Dr. Ronaldo Carlotto Batista

Dissertação de mestrado apresentada ao Instituto de Física da Universidade de São Paulo, como requisito parcial para a obtenção do título de Mestre(a) em Ciências.

Banca Examinadora:
Prof(a). Dr. Edivaldo Moura Santos - Orientador (IF-USP)
Prof(a). Dr(a). Nome do(a) Professor(a) (instituição de trabalho)
Prof(a). Dr(a). Nome do(a) Professor(a) (instituição de trabalho)

São Paulo
2024

FICHA DA BIBLIOTECA

University of São Paulo
Physics Institute

Cosmological Constraints using the Sachs-Wolfe Integrated Effect

Arthur Diniz Meirelles

Supervisor: Prof. Dr. Edivaldo Moura Santos
Co-supervisor: Prof. Dr. Ronaldo Carlotto Batista

Dissertation submitted to the Physics Institute of the University of São Paulo in partial fulfillment of the requirements for the degree of Master of Science.

Examining Committee:
Prof. Dr. Edivaldo Moura Santos - Supervisor (IF-USP)
Prof. Dr. Name (institution)
Prof. Dr. Name (institution)

São Paulo
2024

Frase bonita

Acknowledgements

testando

testando mais

Abstract

ABSTRACT AQUI

Keywords:

Resumo

RESUMO AQUI

Palavras-chave:

List of Figures

LIST OF FIGURES

List of Tables

Contents

1 | Introduction

The discovery of the Cosmic Microwave Background (CMB) is a fine example of serendipity, Arno A. Penzias and Robert W. Wilson found an unexpected excess temperature while measuring the effective zenith noise temperature in 1964, and after some investigation, they attributed this excess temperature to an isotropic radiation field that today we call the CMB [1]. The CMB has since been used as one of the main probes to studying cosmology, being able to provide various tests and insights into cosmological models [2–4] and measurements of cosmological parameters [5, 6].

In the standard cosmological model, commonly called the ΛCDM model, the CMB is a radiation field that has permeated the Universe since the Big Bang, its photons have been freely traveling the Universe since their decoupling from electrons and protons during the very early stages of the Universe's history [7]. The current measurement for the black body spectrum temperature of the CMB is $2.725\,48(57)\,\mathrm{K}$ [8], and despite being isotropic to many orders of precision, it does contain anisotropies in the order of $10^{-5}\,\mathrm{K}$, which is expected in the ΛCDM model [9]. These fluctuations are the result of many physical effects that contribute to the CMB's emission or are acting on the photons as they travel through the Universe, making them an excellent probe to constrain cosmological parameters.

Some mappings of the CMB were carried out in the last few decades, the first satellite launched specifically dedicated to doing this was the Cosmic Background Explorer (COBE) satellite with a $7°$ angular resolution [10], followed by the Wilkinson Microwave Anisotropy Probe (WMAP) with a $0.3°$ angular resolution, which was also able to show that CMB photons are polarized, a property related to other physical effects that assisted cosmologists in further understanding the history of the Universe[11–13]. In 2009, the Planck Satellite was launched, improving upon WMAP's precision to an impressive value of 5' ($\sim 0.083°$) angular resolution [14], allowing cosmologists to access the finest details in the CMB anisotropies to this day. Figure 1.1 shows a comparison between the resolution of these maps.

Amongst the many effects that affect the CMB, the Integrated Sachs-Wolfe (ISW) Effect is one of the most important ones. First described by Rainer K. Sachs and Arthur M. Wolfe in 1967, the ISW effect is a mechanism that causes photons (including CMB photons) to blueshift

Figure 1.1: Each image represents the same 10 square degree patch of the sky measured by the three telescopes shown above each image, the improvement in the resolution of each map is very noticeable. Credit: NASA/LAMBDA Science Team.

in cosmological periods when gravitational potentials change rapidly. One such period is the time between the current dark energy dominated era and the dark matter dominated era before it. During this transition, gravitational potentials decay (or "flatten") over time, causing CMB photons that entered potential wells with a certain gravitational blueshift to leave these wells with a redshift that does not compensate for the initial blueshift, leaving a net blueshift in these photons, creating patterns that can be observed in the CMB temperature map and spectrum[15].

ILUSTRAÇÃO DO ISW?

There are two contributions to the ISW effect: The early-time ISW effect occurs immediately after the last scattering surface (COMPLEMENTAR AQUI DEPOIS), and the late-time ISW effect, which is more recent, occurring in the current dark energy dominated era.

From this association between blueshifted CMB photons and gravity wells, it is natural to assume that the matter distribution of the Universe should hold a statistical cross-correlation between with the CMB temperature map. When looking at the theoretical model, we will see that this cross-correlation is expected, and many works in the past have already searched and found such cross-correlation (EXAMPLE REFS) (COMPLETAR AQUI, VOU COMPLEMENTAR NISSO? APRESENTAR ALGO NOVO? ETC).

The present work expands on a method (what characterizes this method and sets it apart from other ones?) presented in [16] to estimate these cross-correlations, using the models and some techniques presented there, with a more thorough selection of the data that is to be used in

the analysis, using the newer Planck Satellite data instead of the WMAP data, and applying the method to alternative dark energy models, making it possible to compare them with the ΛCDM model and providing insights about the nature of dark energy.

The rest of this dissertation will be organized as follows: DESCRIBE HOW THE SECTIONS ARE ORGANIZED WHEN THE REST OF THE DISSERTATION IS DONE.

2 | Cosmology's Standard Model

The advent of general relativity in the early 20th century allowed physicists to conceptualize mathematical models of the Universe. Albert Einstein proposed a model for a static Universe using his theory[17], and other Universe models were proposed in the following years. To start this chapter, the fundamental principles of cosmology will be discussed and used to setup a simple background for the Universe, and the specificities of the currently most accepted model for the Universe – the ΛCDM model – will be discussed. After this, we will complement this simple background with finer details and provide a statistical description of cosmological observables that can be used to test our models.

2.1 The Homogeneous Background

2.1.1 Fundamental Observations and Principles

One of the fundamental principles of cosmology is called the Cosmological Principle: at large scales, the Universe is both homogeneous and isotropic. This principle can be used to simplify the description of the energy distribution in the Universe, but it also simplifies the possible metrics that can describe the Universe to those that have constant curvature (a quantity denoted as k), and it can be shown that any space with constant curvature is locally isometric to: The Euclidian flat space ($k = 0$), a hyperspherical space ($k = +1$) or a hyperbolic space ($k = -1$)[18]. The Cosmological Principle has support from a good amount of cosmological observations, such as the CMB[10], the galaxy sky distribution[19, 20], amongst others.

In the period from 1927 to 1929, Edwin Hubble and Georges Lemaître, amongst other scientists, greatly contributed to the current understanding of cosmology: Observations were carried out and showed that most galaxies and nebulae data show a redshift proportional to their distances relative to the earth[21], these results were studied using general relativity and cosmological models at the time[22]. It was then established another principle that physicists were avoiding in their theoretical models for quite some time: The Universe is not static, in fact it is expanding, and for objects not too far (REFERÊNCIA), there is a linear relationship between the redshift of an observed object and its distance to the observer.

To describe the Universe, a coordinate system is embedded in the entire Universe, and to describe its dynamical nature, the scale factor a is introduced to the theoretical model: a is set to 1 at the present as a convention (usually called a_0), and its value at any given time $a(t)$ is the size of the Universe relative to its present size. A simple relation can be established between the scale factor of an observed object and its redshift z:

$$1 + z = \frac{\lambda_{\text{obs}}}{\lambda_{\text{emit}}} = \frac{a_{\text{obs}}}{a_{\text{emit}}} = \frac{1}{a_{\text{emit}}} \tag{2.1}$$

where λ and a are the wavelength of the radiation and the scale factor, respectively, when emitted (λ_{emit} and a_{emit}) and when observed (λ_{obs} and a_{obs}).

$$H(t) = \frac{1}{a}\frac{\mathrm{d}a}{\mathrm{d}t} \tag{2.2}$$

These properties are not exclusive to a particular cosmological model, instead being present in all of them. The standard model of cosmology, called ΛCDM, usually takes a few assumptions on top of the ones described previously:

- The Universe emerged from a space-time singularity that started expanding several billion years ago, in an event called the Big Bang;

- Aside from baryonic matter, radiation and neutrinos, there are two other main components in the Universe: non-relativistic (cold) dark matter and an energy component with constant density called dark energy, which is related to a cosmological constant Λ;

- During the early stages of the Universe's history, it went through a period of rapid acceleration driven by a scalar quantum field.

Based on the Cosmological Principle, most theoretical models first set up a homogeneous and isotropic background description of the Universe, and then introduce perturbations to this background, allowing for a detailed statistical description of its evolution. In the rest of this section, we will use the principles and assumptions just presented to set this background.

2.1.2 Friedmann Equations

As already mentioned, the main theoretical framework to describe the Universe is the theory of general relativity, since the most relevant force in the scale of the Universe is the gravitational one. We then use Einstein's field equations with a cosmological constant Λ:

$$R_{\mu\nu} - \frac{1}{2}g_{\mu\nu}R + \Lambda g_{\mu\nu} = 8\pi G T_{\mu\nu}, \tag{2.3}$$

where $R_{\mu\nu}$ is the Ricci curvature tensor for the Universe's metric $g_{\mu\nu}$, $R \equiv g_{\mu\nu}R^{\mu\nu}$ is the Ricci scalar, G is the gravitational constant and $T_{\mu\nu}$ is the energy-momentum tensor.

In equation (2.3) and throughout this text (unless otherwise stated), we will use units such that the Boltzmann constant (k_b), the speed of light in a vacuum (c) and the reduced Planck constant ($\hbar$) are all equal to one. Furthermore, Greek letter tensor indices indicate that the time component of the tensor is included in the equation and Latin letter tensor indices indicate that only spatial components are included. Current results strongly indicate the metric $g_{\mu\nu}$ of the Universe to be flat ($k = 0$)[6], thus justifying the use of an Euclidian metric scaled by $a(t)$, and we will assume a homogeneous and isotropic distribution of energy throughout the Universe to construct an energy-momentum tensor with constant energy density ρ_0 and constant pressure P[23]:

$$g_{\mu\nu} = \begin{pmatrix} -1 & 0 & 0 & 0 \\ 0 & a^2 & 0 & 0 \\ 0 & 0 & a^2 & 0 \\ 0 & 0 & 0 & a^2 \end{pmatrix} \qquad T_{\mu\nu} = \begin{pmatrix} -\rho_0 & 0 & 0 & 0 \\ 0 & P & 0 & 0 \\ 0 & 0 & P & 0 \\ 0 & 0 & 0 & P \end{pmatrix}. \tag{2.4}$$

The metric $g_{\mu\nu}$ described in equation (2.4) is called the Friedmann-Lemaître-Robertson-Walker (FLRW) metric[24]. In order to expand any equation from (2.3), it is necessary to determine $R = g^{\mu\nu}R_{\mu\nu}$. By expanding the expression using the matrices defined in (2.4), the result is

$$R = 6\left[\frac{\ddot{a}}{a} + \left(\frac{\dot{a}}{a}\right)^2\right]. \tag{2.5}$$

From all the equations in (2.3), if the one corresponding to $\mu = \nu = 0$ is expanded using the

result (2.5), one obtains

$$\left(\frac{\dot{a}}{a}\right)^2 = \frac{1}{3}\left(8\pi G\rho_0 + \Lambda\right),\tag{2.6}$$

which relates the relative rate at which the Universe is expanding with the energy content of the Universe. In the ΛCDM model, Λ is assumed to be the source of the current accelerated expansion of the Universe, so an energy component related to this constant is necessary, and its energy density can be defined as

$$\rho_\Lambda = \frac{\Lambda}{8\pi G},\tag{2.7}$$

such that

$$\left(\frac{\dot{a}}{a}\right)^2 = \frac{8\pi G}{3}\rho,\tag{2.8}$$

where $\rho = \rho_\Lambda + \rho_0$. This is called Friedmann's first equation.

When any of the space-space equations of (2.3) is expanded and the resulting equation is combined with equation (2.8), Friedmann's second equation is obtained:

$$\frac{\ddot{a}}{a} = -\frac{4\pi G}{3}(\rho + 3P).\tag{2.9}$$

This equation is a relation between the acceleration of the Universe and its energy content. It is clear that $P < -\frac{1}{3}\rho$ indicates a Universe expanding with a positive acceleration, which is highly unexpected since gravity is an attractive force, but in section 2.1.3 the case of the cosmological constant will be discussed, in which Λ yields $P_\Lambda = -\rho_\Lambda$, being the reason it contributes to an accelerated expansion.

2.1.3 Energy Content

To understand the contribution of each component of the Universe to its dynamics, a differential equation for each component has to be determined, we do this using the energy-momentum conservation equation:

$$\nabla_\mu T^\mu_\nu \equiv \partial_\mu T^\mu_\nu + \Gamma^\mu_{\alpha\mu}T^\alpha_\nu - \Gamma^\alpha_{\nu\mu}T^\mu_\alpha = 0.\tag{2.10}$$

Again using the energy-momentum tensor defined in (2.4), the following equation is obtained:

$$\frac{\partial \rho}{\partial t} + \frac{\dot{a}}{a}(3\rho + 3P) = 0. \tag{2.11}$$

To solve this, a relation between density and pressure for each component of the Universe is needed, an equation of state. It is commonly assumed that, for a given component s of the Universe, its equation of state takes the form

$$P_s = w_s \rho_s, \tag{2.12}$$

where w_s is called the equation of state parameter. Using that equation and solving for $\rho_s(a)$ on equation (2.11) yields

$$\rho_s(a) \propto \exp\left[-3\int_1^a \frac{da'}{a'}[1 + w_s(a')]\right]. \tag{2.13}$$

This solution ignores further interaction between components, it would apply to a single-component Universe, but it is also a useful first approximation in epochs of dominance of a single component. In the ΛCDM model, it is assumed that all components of the Universe possess a constant value for w_s, in that case the solution is simple:

$$\rho_s(a) \propto a^{-3(1+w_s)}. \tag{2.14}$$

This represents the evolution of the density parameter of any component as a function of the scale parameter, and thus as a function of cosmological time, since $a(t)$ is monotonically increasing (the Universe has not reduced at any point in its history so far).

The rigorous form of determining w_s for some components of the Universe requires the usage of statistical physics. In cases where we have limited information on the physical properties of a certain component, such as dark energy, theoretical frameworks and assumptions have to be used, as well as the analysis of data.

In the case of dark energy, assuming its origin is related to the cosmological constant, the data strongly suggests a value of $w_\Lambda = -1$, which also indicates a constant density for dark energy. From the quantum field theory point of view, the cosmological constant energy density would be associated to zero point energy of a quantum field. However, so far, no calculation has been

successful in predicting a zero point energy whose density is consistent with the cosmological observations[25]. Many models propose alternative possibilities, such as dynamical dark energy in which w_{DE} is a function of a[26], which would still be able to explain the accelerated expansion of the Universe as long as $w_{DE} < -\frac{1}{3}$, these are discussed in more detail in section 2.5. Table 2.1 summarizes the equation of state properties of each known component in the Universe.

It is very useful to also define the energy density fraction of each component of the Universe using

$$\Omega_s = \frac{\rho_s(a_0)}{\rho_{\text{crit}}}, \tag{2.15}$$

where ρ_{crit} is the so called critical density, defined as

$$\rho_{\text{crit}} \equiv \frac{3H_0^2}{8\pi G} \approx 8.5 \times 10^{-27} \, \text{kg/m}^3, \tag{2.16}$$

where H_0 is the Hubble constant, the value of the Hubble parameter $H(t)$ defined in (2.2) at the present.

This energy density makes it possible to determine what is the curvature of the Universe: if the total sum of energy densities in the Universe is equal to the critical density, the Universe is flat; if this sum is higher than ρ_{crit} the Universe would have positive curvature; and if this sum is lower than ρ_{crit}, the Universe would have negative curvature[27].

Table 2.1 summarizes the current estimated values for these energy fractions for the Universe in the present. It is important to note that commonly in cosmology (and throughout this text), the classification of baryons includes electrons, even though, according to the standard model of particle physics, electrons belong, together with their associated neutrinos, to one of the three families of leptons.

2.1.4 A Brief History of the Universe

We commonly categorize different stages of the Universe according to important events that happened during its history. The ΛCDM model assumes the Universe started as a singularity; as it started expanding, quantum fluctuations at that time would eventually result in inhomogeneities thought to be the source for the formation of structures.

Component	$\rho(a)$	w	Ω
Baryonic matter	$\rho_0 a^{-3}$	0	0.05
Cold dark matter	$\rho_0 a^{-3}$	0	0.26
Radiation	$\rho_0 a^{-4}$	$\frac{1}{3}$	5.29×10^{-5}
Dark energy	ρ_0	-1	0.68
Curvature	$\rho_0 a^{-2}$	$-\frac{1}{3}$	0.001

Table 2.1: Equation of state parameters w, energy density functions $\rho(a)$ and energy density fractions for each known component of the Universe according to the ΛCDM model. Most data were adapted from Planck[6], the radiation data was calculated based on [28].

The next important period of the Universe's evolution was a highly accelerated expansion epoch driven by an effect called cosmic inflation, first proposed as a solution to the horizon problem[29, 30], related to how can the CMB temperature differences across the sky be so small ($\sim 10^{-5}$ K), even between points apparently causally disconnected during all epochs of the Universe's thermal history. The ΛCDM model assumes inflation was driven by a quantum scalar field[23]. Definitive evidence of the inflationary model may be reached with the detection of a certain type of polarization of the CMB called the B-modes, which have not been detected yet, but have reached good constraints.[13]

Briefly after inflation, baryons and photons are still coupled through Compton scattering, thus photons are still unable to travel freely. The Universe at this point is composed of photons coupled with baryons, helium nuclei, and trace amounts of lithium. With the decrease in temperature, hydrogen atoms can form without being quickly ionized, Compton scattering eventually can no longer maintain baryons and photons coupled, resulting in a decoupling of these components. The photons are released to travel across the Universe, the radiation field formed from this period is what we currently measure as the CMB.

After this, an epoch called "the Dark Ages" starts, in which the photons in the Universe are the result of the decoupling described before and stars are yet to be formed, which is the reason why it is called a dark age. Matter dominates this period, greatly decreasing the rate of expansion of the Universe. As a result of the quantum fluctuations in the early Universe, stars, galaxies, and other structures form. The study of the formation of structure is completely dependent on the study of the inhomogeneities of the Universe at small scales, where the cosmological principle is no longer expected to be valid. Some details of this theoretical framework will be covered in the next section.

Figure 2.1 shows a summarized and visual representation of some of the events described in

this section.
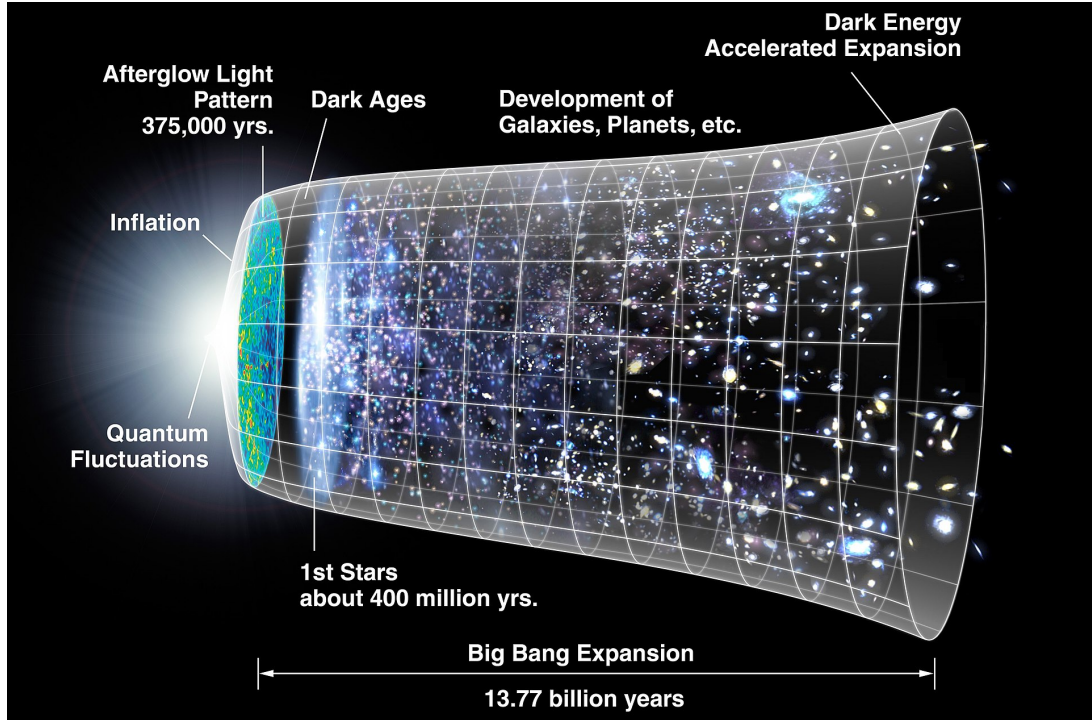
Figure 2.1: A representation of the time evolution of the Universe, starting from the left (the Big Bang) with time passing towards the right. The radius of each section indicates the size of the Universe at that time; during inflation this radius increases very rapidly, indicating an accelerated expansion during this period, while closer to the present the slope of increase in size shows a slight acceleration, indicating the current dark energy accelerated period. Briefly after the inflation period (in cosmological time), the photons decouple from baryons, leaving a radiation field in the Universe, resulting in the CMB, represented in the image by the afterglow of inflation. After this, the only radiation in the Universe is this afterglow for many years, during that time structure starts to form from the small inhomogeneities left by quantum fluctuations in the very early stages of the Universe, forming the first stars and then the first galaxies. Credit: NASA/WMAP Science Team.

2.2   Inhomogeneities and Anisotropies

The existence of structures – nebulae, stars, galaxies, clusters – in the Universe indicates that, throughout its history, it has been inhomogeneous and anisotropic at some scale. These perturbations to the uniform background are relatively small though, take the CMB for instance: CMB anisotropies are around 5 orders of magnitude lower than its average blackbody temperature[5].

In this scenario, there is no known theoretical model that can predict the exact behavior of every particle in the Universe. Therefore, we turn to a statistical prediction taking into account

the properties of space-time and the components of the Universe. In this section, the first order equations that govern these properties will be shown by introducing perturbations both to the metric and to the stress-energy tensor.

2.2.1 Perturbed Space-Time

In the ΛCDM model, to account for perturbations in the uniform background previously set, we use the following new form for the metric:

$$
\begin{cases}
g_{00} = -1 - 2\Psi(\mathbf{x}, t), \\
g_{0i} = g_{i0} = 0, \\
g_{ij} = a^2(t)\delta_{ij}[1 + 2\Phi(\mathbf{x}, t)].
\end{cases}
\tag{2.17}
$$

In equation (2.17), Ψ corresponds to the Newtonian potential and governs the movement of nonrelativistic objects[23], while Φ is a perturbation to the spatial curvature.

With the use of the geodesic equation on this new tensor and using a first order approximation, it is possible to obtain the following results for the motion equations of particles traveling through the perturbed space-time:

$$
\frac{\mathrm{d}x^i}{\mathrm{d}t} = \frac{\hat{p}_i}{a}\frac{p}{E}(1 - \Phi + \Psi),
\tag{2.18}
$$

$$
\frac{\mathrm{d}p^i}{\mathrm{d}t} = -(H + \dot{\Phi})p^i - \frac{E}{a}\partial_i\Psi - \frac{1}{a}\frac{\mathrm{d}p^i}{\mathrm{d}E}p^k\partial_k\Phi + \frac{p^2}{aE}\partial_i\Phi.
\tag{2.19}
$$

We can use

$$
\frac{\mathrm{d}p}{\mathrm{d}t} = \frac{\mathrm{d}}{\mathrm{d}t}\sqrt{\delta_{ij}p^ip^j} = \delta_{ij}\frac{p^i}{p}\frac{\mathrm{d}p^j}{\mathrm{d}t}
\tag{2.20}
$$

and $\hat{p}^i = p^i/p$ in combination with equation (2.19) to find separate equations for p and $\hat{p}^i$:

$$
\frac{\mathrm{d}p}{\mathrm{d}t} = -[H + \dot{\Phi}]p - \frac{E}{a}\hat{p}^i\partial_i\Psi,
\tag{2.21}
$$

$$
\frac{\mathrm{d}\hat{p}^i}{\mathrm{d}t} = \frac{E}{ap}[\delta^{ik} - \hat{p}^i\hat{p}^k]\partial_k\left(\frac{p^2}{E^2}\Phi - \Psi\right).
\tag{2.22}
$$

As for the dynamics of the field perturbations, it is possible to use Einstein's field equations to

obtain, in Fourier space, the equations for scalar perturbations on the gravitational potentials[23]

$$k^2\Phi + 3H(\dot{\Phi} - H\Psi) = -4\pi G a^2(\rho_{DM}\delta_{DM} + \rho_b\delta_b + 4\rho_\gamma\Theta_0 + 4\rho_\nu\mathcal{N}_0), \tag{2.23}$$

$$k^2(\Phi + \Psi) = -32\pi G a^2(\rho_\gamma\Theta_2 + \rho_\nu\mathcal{N}_2). \tag{2.24}$$

Here, ρ indicates the average density of a component, δ represents the perturbation to these densities, and the indexes DM, b, γ and ν indicate the quantities related to dark matter, baryons, radiation and neutrinos respectively. The terms Θ_0, Θ_2, $\mathcal{N}_0$ and $\mathcal{N}_2$ are obtained in the calculation of the perturbed energy-momentum tensor, they are defined as

$$F_\ell = \frac{1}{(-i)^\ell} \int_{-1}^{1} \frac{\mathcal{P}_\ell(\mu)F(\mu)}{2} d\mu, \tag{2.25}$$

where F can either represent Θ or $\mathcal{N}$; $\mu = \hat{k} \cdot \hat{p}$ is the cosine between the momentum direction of the photon and the Fourier space wavevector; $\mathcal{P}_\ell$ are Legendre polynomials; the functions $\Theta(\mu)$ and $\mathcal{N}(\mu)$ are dimensionless fields that quantify the perturbations of photon and neutrino distributions with respect to the homogeneous background; and i is the imaginary unit $i^2 = -1$.

2.2.2 The Boltzmann Equation

The Boltzmann equation is a fundamental component in the study of every component of the Universe. One general form of writing the Boltzmann equation is

$$\frac{\mathrm{d}f}{\mathrm{d}t} = \frac{\partial f}{\partial t} + \frac{\partial f}{\partial x^i} \cdot \frac{\mathrm{d}x^i}{\mathrm{d}t} + \frac{\partial f}{\partial p}\frac{\mathrm{d}p}{\mathrm{d}t} + \frac{\partial f}{\partial \hat{p}^i} \cdot \frac{\mathrm{d}\hat{p}^i}{\mathrm{d}t} = C[f], \tag{2.26}$$

where f is the distribution function of the component to be analyzed and $C[f]$ is the collision term, a factor that is calculated by considering the interactions of such components.

Using equations (2.21) and (2.22) with the Boltzmann equation and assuming $E = p$, i.e. assuming a relativistic particle such as photons, the full first order Boltzmann equation for photons is

$$\begin{aligned}
\frac{\mathrm{d}f}{\mathrm{d}t} =& \frac{\partial f}{\partial t} + \frac{\partial f}{\partial x^i}\frac{\hat{p}^i}{a}(1 - \Phi - \Psi) - \frac{\partial f}{\partial p}\left\{[H + \dot{\Phi}]p + \frac{1}{a}p^i\partial_i\Psi\right\} \\
&+ \frac{\partial f}{\partial \hat{p}^i}\frac{1}{a}\left[\partial_i(\Phi - \Psi) - \hat{p}^i\hat{p}^k\partial_k(\Phi - \Psi)\right].
\end{aligned} \tag{2.27}$$

The first order approximation is being used, and so it is possible to simplify this expression further. For instance, the distribution f for the homogeneous background takes the form of Bose-Einstein's distribution, which means there is no dependence on $\hat{p}^i$ and x^i in this case. It is commonly assumed that the deviations from this distribution are of the same order of the perturbations Φ and Ψ, so both $\frac{\partial f}{\partial x^i}$ and $\frac{\partial f}{\partial \hat{p}^i}$ are first order factors, multiplied by Φ or Ψ result in second order terms which can be neglected, resulting in

$$\frac{\mathrm{d}f}{\mathrm{d}t} = \frac{\partial f}{\partial t} + \frac{\hat{p}^i}{a}\frac{\partial f}{\partial x^i} - \left[H + \dot{\Phi} + \frac{1}{a}\hat{p}^i\partial_i\Psi\right]p\frac{\partial f}{\partial p}. \tag{2.28}$$

This is an important equation for the description of the CMB, but the description of anisotropies for massive particles is still important, for which the same assumptions are made, resulting in

$$\frac{\mathrm{d}f}{\mathrm{d}t} = \frac{\partial f}{\partial t} + \frac{p}{Ea}\hat{p}^i\frac{\partial f}{\partial x^i} - \left[H + \dot{\Phi} + \frac{E}{ap}\hat{p}^i\partial_i\Psi\right]p\frac{\partial f}{\partial p}. \tag{2.29}$$

The only difference between these equations is the term E/p which, in the case of radiation, is equal to 1. The first order approximation for non-relativistic matter breaks down in the late Universe, a non-linear model is necessary in this scenario.

To arrive at a differential equation, a function to describe the perturbations needs to be defined, and so does the distribution function. Taking the CMB as an example, the perturbed form of the temperature distribution for CMB photons in general can be defined as

$$T(\mathbf{x}, \hat{\mathbf{p}}, t) = \bar{T}(t)[1 + \Theta(\mathbf{x}, \hat{\mathbf{p}}, t)], \tag{2.30}$$

where $\bar{T}$ is the average temperature in a given time and Θ is the same field presented in equation (2.25), that quantifies the perturbations of the CMB distribution with respect to its average value. This perturbation field can be expressed in terms of the set of functions Θ_ℓ defined in (2.25) by the following equation in Fourier space:

$$\Theta(\hat{\mathbf{k}}, \mu) = \sum_{\ell=0}^{\infty}(2\ell + 1)(-i)^\ell\Theta_\ell(\hat{\mathbf{k}})\mathcal{P}_\ell(\mu). \tag{2.31}$$

If we use the Bose-Einstein distribution for the temperature defined in (2.30) and expand it to its first order, we obtain

$$f(\mathbf{x}, \mathbf{p}, t) = f^{(0)}(p, t) - p\frac{\partial f^{(0)}(p, t)}{\partial p}\Theta(\mathbf{x}, \mathbf{p}, t), \tag{2.32}$$

where

$$f^{(0)}(p, t) = \left[\exp\left(\frac{p}{T}\right) - 1\right]^{-1} \tag{2.33}$$

We can then expand the Boltzmann equation using the results in (2.32) and (2.33) and take into account Compton scattering to calculate the collision term $C[f]$ to obtain a differential equation for the CMB photons. We can use similar procedures, using adequate distribution functions, and obtain a set of coupled differential equations to describe the evolution of the perturbations of every known component of the Universe in Fourier space[23]:

$$\dot{\Theta} + ik\mu\Theta = -\dot{\Phi} - ik\mu\Psi - \dot{\tau}\left[\Theta_0 - \Theta + \mu v_b - \frac{1}{2}\mathcal{P}_2(\mu)(\Theta_2 + \Theta_{P2} + \Theta_{P0})\right], \tag{2.34}$$

$$\dot{\Theta}_P + ik\mu\Theta_P = -\dot{\tau}\left\{-\Theta_P + \frac{1}{2}[1 - \mathcal{P}_2(\mu)](\Theta_2 + \Theta_{P2} + \Theta_{P0})\right\}, \tag{2.35}$$

$$\dot{\delta} + ikv = -3\dot{\Phi}, \tag{2.36}$$

$$\dot{v} + Hv = -ik\Psi, \tag{2.37}$$

$$\dot{v}_b + Hv_b = -ik\Psi + \frac{4\rho_\gamma}{3\rho_b}\dot{\tau}(v_b + 3i\Theta_1), \tag{2.38}$$

$$\dot{\mathcal{N}} + ik\mu\mathcal{N} = -\dot{\Phi} - ik\mu\Psi. \tag{2.39}$$

Here, Θ_P is the polarization field and $\Theta_{P\ell}$ is defined by equation (2.25) using $F = \Theta_P$; δ and δ_b are the perturbations to the matter and baryon distributions respectively; v and v_b are the bulk velocities of the fluids in the stress-energy tensor for matter and baryons respectively; ρ_b and ρ_γ are the baryon and radiation energy densities respectively; and τ is the optical depth of the Universe.

These equations, alongside equations (2.23) and (2.24), are very complex to be solved analytically, so it is common to evolve them numerically, and there are a few codes developed specifically to do this. One of them, that has been used in this project, is CAMB.[31, 32]

2.3   The Cosmic Microwave Background

With the dynamical equations for photons determined, one can obtain the temperature pertur-
bation distribution Θ if initial conditions are provided. With the equations already presented,
it is possible to show that the initial conditions at the early Universe depend only on the initial
conditions for Φ[23], which are then evolved through the inflationary period assuming the
existence of a quantum scalar field $\phi(\mathbf{x}, t)$ that drives a brief accelerated expansion.

With time, particles start to form: Quarks, hadrons, neutrinos, amongst others, at different
times. Eventually baryons have formed and the photons are tightly coupled to them, forming a
baryon-photon fluid that can be described by the differential equations (2.34) - (2.39), the initial
distribution obtained for this fluid can then be used as the initial condition and evolved to predict
the present anisotropies to the uniform background. To analyze these predictions, the statistical
behavior of each component of the Universe is taken: either their spectral densities – usually
called their power spectra – or what is known as their correlation spectra.

2.3.1   CMB Autocorrelation Spectrum

Equation (2.30) explicitly assumes a dependence in position, time, and momentum direction.
Measurements made on Earth can assume a fixed value for time since our measurements related
to the Universe are taken in a period negligible in the cosmological scale, but the translational
movement of the Earth is relevant to our measurements: measurements of the CMB made by
a non-comoving observer, when projected onto a sphere, lead to a strong dipole pattern in the
temperature distribution, modulation of the multipole terms and a small relativistic aberration at
angular scales of a few arcminutes[33–35].

Despite these effects, measurements of the temperature distribution can be projected onto a
sphere independent of the Earth's position, making it possible to describe this distribution simply
using two angle variables, or simply $\hat{\mathbf{p}}$.

We can expand the temperature perturbations in spherical harmonics:

$$\Theta(\mathbf{x}, \hat{\mathbf{p}}, t) = \sum_{\ell=1}^{\infty} \sum_{m=-\ell}^{\ell} a_{\ell m}(\mathbf{x}, t) Y_{\ell m}(\hat{\mathbf{p}}). \tag{2.40}$$

All the information about temperature maps of the CMB measured on Earth are contained in

the set of $a_{\ell m}$ values. Given the limited number of pixels N_{pix} of any of these maps, there is a maximum value of ℓ (ℓ_{max}) up to which statistically meaningful information can be retrieved. For each value of ℓ, there are $2\ell + 1$ values of m – and $a_{\ell m}$ – in the series, a hypothetical observed map with precision p_r in squared radians would have $4\pi/p_r$ pixels, setting this number of pixels equal to the number of $a_{\ell m}$ used to describe this map gives a reasonable estimation of ℓ_{max}[23], so

$$\sum_{\ell=0}^{\ell=\ell_{\text{max}}} (2\ell + 1) = (\ell_{\text{max}} + 1)^2 = N_{\text{pix}} = \frac{4\pi}{p_r}. \tag{2.41}$$

Using the orthogonality property of the spherical harmonics, one can obtain a direct expression for $a_{\ell m}$ in terms of the angular distribution of the perturbations:

$$a_{\ell m}(\mathbf{x}, t) = \int \frac{d^3 k}{(2\pi)^3} e^{i\mathbf{k}\cdot\mathbf{x}} \int d\Omega Y_{\ell m}^*(\hat{\mathbf{p}}) \Theta(\mathbf{k}, \hat{\mathbf{p}}, t). \tag{2.42}$$

Again, there are available codes that efficiently and precisely calculate $a_{\ell m}$ from a pixelized map and vice versa, the one used in this work was HEALPix[36]. Under the hypothesis that the spherical harmonics coefficients $a_{\ell m}$ are independent Gaussian random variables with zero mean, all its statistical properties are contained in the variance C_ℓ, also known as the power spectrum:

$$\langle a_{\ell m} a_{\ell' m'}^* \rangle = \delta_{\ell \ell'} \delta_{mm'} C(\ell), \tag{2.43}$$

where $\delta_{mm'}$ is the Kronecker delta taking m and m' as arguments.

The fact that for lower values of ℓ there are fewer coefficients $a_{\ell m}$ naturally leads to lower multipoles ℓ having higher uncertainty, this property is usually called cosmic variance and can be expressed using[23]

$$\left(\frac{\Delta C(\ell)}{C(\ell)}\right)_{\text{cosmic variance}} = \sqrt{\frac{2}{2\ell + 1}}. \tag{2.44}$$

The temperature autocorrelation defined in equation (2.43) is usually expressed as C_ℓ^{TT}, but sometimes a modified spectrum $D_\ell^{TT} = \frac{\ell(\ell+1)}{2\pi} C_\ell^{TT}$ is used for visualization purposes. Figure 2.2 shows Planck's CMB power spectrum data and its corresponding best-fit spectrum assuming a ΛCDM cosmology.
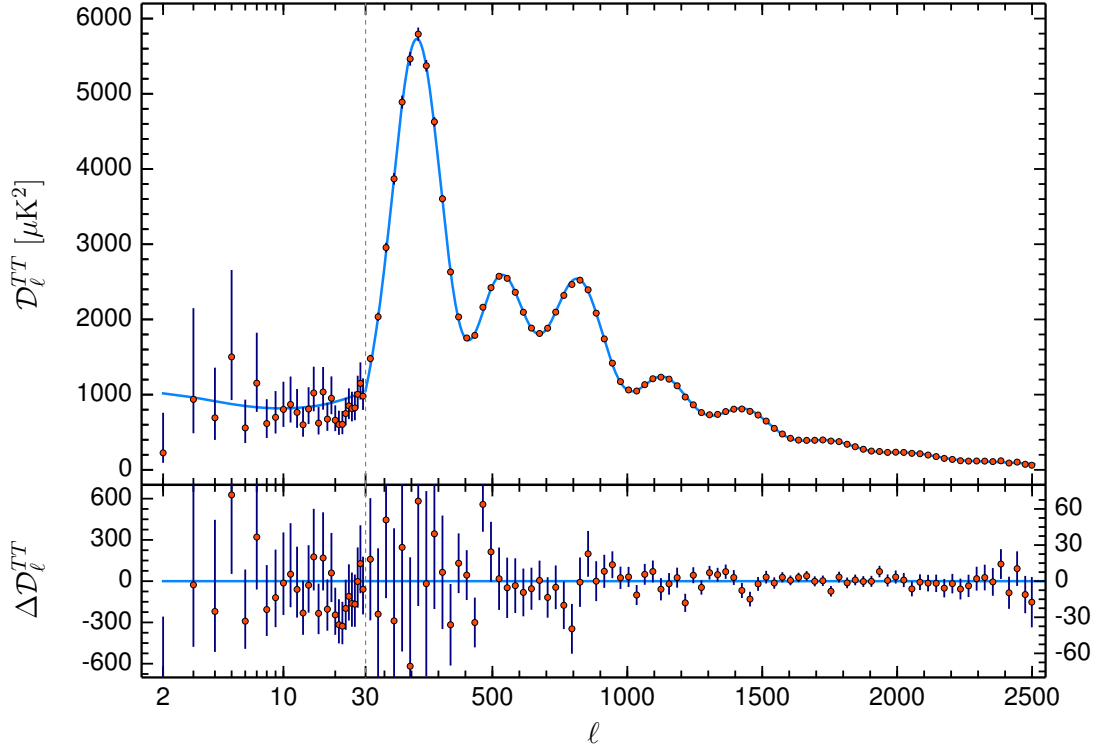
Figure 2.2: Planck 2018 CMB temperature power spectrum: the blue line corresponds to a ΛCDM cosmology best-fit to the data points in orange. For $\ell < 30$ a logarithmic scale was used and the data points correspond to the D_ℓ^{TT} for each value of ℓ, while for $\ell \geq 30$ a linear scale was used and the data points correspond to binned values for the data for D_ℓ^{TT}. The error bars show $\pm 1\sigma$ uncertainties, including cosmic variance. Extracted from [6].

2.3.2 Analytical Approximation

Although solving equations such as (2.34) numerically gives accurate results, obtaining an analytical approximation to these equations helps us understand the underlying physical effects that most influence the evolution of the perturbations. Working on the tightly coupled limit and assuming recombination to be an instantaneous process happening at conformal time $\eta = \eta_*$, one can obtain the following equation[23]:

$$
\begin{aligned}
\Theta_\ell(k, \eta_0) \approx & [\Theta_0(k, \eta_*) + \Psi(k, \eta_*)] j_\ell[k(\eta_0 - \eta_*)] \\
& + i v_b(k, \eta_*) \left\{ j_\ell[k(\eta_0 - \eta_*)] - (l+1) \frac{j_\ell[k(\eta_0 - \eta_*)]}{k(\eta_0 - \eta_*)} \right\} \\
& + \int_0^{\eta_0} d\eta\, e^{-\tau} [\Psi'(k, \eta) - \Phi'(k, \eta)] j_\ell[k(\eta_0 - \eta)],
\end{aligned}
\tag{2.45}
$$

where j_ℓ are spherical Bessel functions, the conformal time η is defined as

$$\eta = \int_0^t \frac{dt}{a(t)}, \tag{2.46}$$

and η_* is the value of η that maximizes the visibility function $g(\eta)$:

$$g(\eta) = -\tau' e^{-\tau}. \tag{2.47}$$

With these conventions, the derivative with respect to η is being represented by the apostrophe notation, while the dot notation used in equation (2.34) will still indicate derivatives with respect to time.

There are three main contributors to the solution (2.45):

- The $(\Theta_0 + \Psi)$ term is usually called the Sachs-Wolfe term, which is associated with Baryon Acoustic Oscillations (BAO), which are fluctuations in the density of the visible baryonic matter of the Universe, caused by acoustic density waves in the primordial plasma of the early Universe[23];

- The iv_b term shows a contribution to the spectrum related to a Doppler shift of the BAO, due to its dependence on a non-zero bulk velocity of the baryons during recombination;

- The last term, an integral involving the time variations of the gravitational potentials, represents the Integrated Sachs-Wolfe (ISW) effect. Its dependence on the variation of the gravitational potential makes it so that it only has a non-negligible effect on the CMB at cosmological periods with high variation of these potentials: At around $a \approx 10^{-4}$ the Universe transitioned from a radiation-dominated to a matter-dominated Universe (early ISW), and recently – around $a \approx 0.61$ or $z \approx 0.63$[37] according to the ΛCDM model – the Universe transitioned from a matter-dominated Universe to the current dark energy dominated Universe (late ISW).

2.4   The Integrated Sachs Wolfe Effect

It was proposed that the cross-correlation spectrum between CMB maps and matter contrast could be used to detect the ISW effect[38], and since then many works have reported the

detection of this signal[39–42]. In this section, a framework for theoretical estimations of the ISW contribution to this cross-correlation will be discussed.

2.4.1   The Matter Power Spectrum

While the CMB is usually described as a two dimensional map measured around the Earth, the matter distribution in the Universe is first analyzed taking the distance from the Earth into consideration, so three coordinates are necessary, and then one can take a 2D projection for a certain redshift z. Again using Fourier space, we first define the 3D matter power spectrum for the distribution of matter perturbations in the Universe $P(k)$ as

$$\langle \delta(\mathbf{k}, z)\delta^*(\mathbf{k}', z)\rangle = (2\pi)^3 P(k, z)\delta_D(\mathbf{k} - \mathbf{k}'), \tag{2.48}$$

where δ_D is the Dirac delta, δ is the previously shown matter perturbation distribution in the Universe and the $*$ superscript indicates the complex conjugate of a quantity. Again, using appropriate initial conditions, one can determine $\delta(\mathbf{k})$ and thus $P(k, z)$, and again these results can be obtained numerically using CAMB, Figure 2.3 shows the results for this calculation using the HALOFIT model[43], a semi-analytical method to determine a non-linear solution for $P(k, z)$.

2.4.2   The Galaxy-CMB Correlation Spectra

To obtain the autocorrelation for a spherical projection of a matter density distribution on a spherical shell on a certain redshift z, one has to choose a way to trace the matter density with an observable. One way of doing this is by tracing the mass distribution with galaxy density on a certain redshift. It is common to assume that the galaxy density perturbations, usually called galaxy contrast maps, take the form $\delta_g = b_g\delta$ where b_g is a constant value (for each redshift z) called the bias factor. From this point, the same process needed to calculate (2.43) can be applied: Expand the distribution in spherical harmonics with factors $a_{\ell m}^g$ and calculate the variance of these variables to obtain an autocorrelation spectrum $C^{gg}(\ell)$.

Similarly, instead of calculating an autocorrelation spectrum, one can calculate a cross-correlation between two perturbation distributions, which is analogous to definition (2.43):
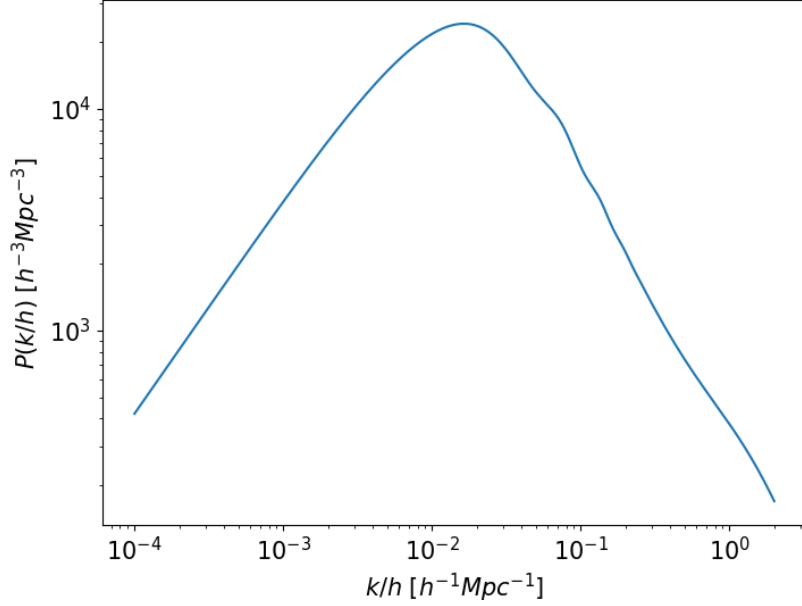
Figure 2.3: Matter power spectrum calculated as a function of k/h, where $h = H_0/(100\,\text{km/s/Mpc})$, using the HALOFIT model with cosmological parameters according to Planck's best fit results[6].

$$\left\langle a^t_{\ell m} a^g_{\ell' m'} \right\rangle = C^{tg}_\ell \delta_{\ell\ell'} \delta_{mm'}. \tag{2.49}$$

One can determine a general and direct equation to calculate these spectra. In this work we have used the form shown in [16], which is specific to the ISW contribution to these correlation spectra:

$$C^{xy}_\ell = \frac{2}{\pi} \int dk k^2 W^x_\ell(k) W^y_\ell(k) P(k), \tag{2.50}$$

where x and y can represent g or t, and W_ℓ are called the kernel functions, which can be calculated using

$$W^t_\ell = -3\Omega_m \left(\frac{H_0}{k}\right)^2 \int dz \frac{d[(1+z)D(z)]}{dz} j_\ell[k\chi(z)], \tag{2.51}$$

$$W^g_\ell = \int dz b_g(z) \frac{dN}{dz} D(z) j_\ell[k\chi(z)], \tag{2.52}$$

where $D(z)$ is the linear growth function (normalized to 1 at $z = 0$); $\chi(z)$ is the comoving distance; and $\frac{dN}{dz}$ is the normalized galaxy redshift distribution, also called the selection function[39].

A demonstration of this equation can be found in Appendix A

With equation (2.50), we can determine the theoretical spectra for CMB and galaxy autocorrelations and CMB-galaxy cross-correlation directly. Figure 2.4 shows the total CMB autocorrelation and the ISW contribution, both at $z = 0$.
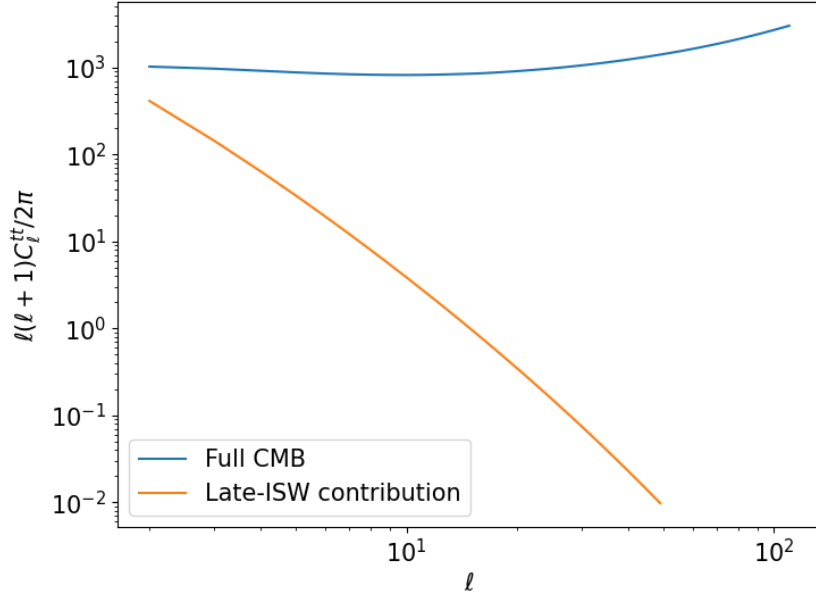
Figure 2.4: CMB autocorrelation comparison for the late-ISW term and the full spectrum. Calculations were made using CAMB (for the full spectrum) and codes developed during the project. The parameters used are those corresponding to the Planck best fit parameters[6].

Figure 2.5 shows the galaxy autocorrelation spectrum and the galaxy-CMB cross-correlation spectrum. All of these spectra have been integrated numerically.

These plots, show very clearly that the ISW effect has a lot more relevance in the lower multipoles, where cosmic variance has a significant influence. The selection function is an important aspect of this signal, in chapter 3 the matter of how to optimize the signal with the use of an idealized selection function will be discussed.

2.5   Dependence on Dark Energy Models

Many approaches to study dark energy have been proposed, each of them with different properties, ranging from parameterization of the equation of state[44, 45] to alternative fluid models for dark energy[46] and modifications to general relativity[47].
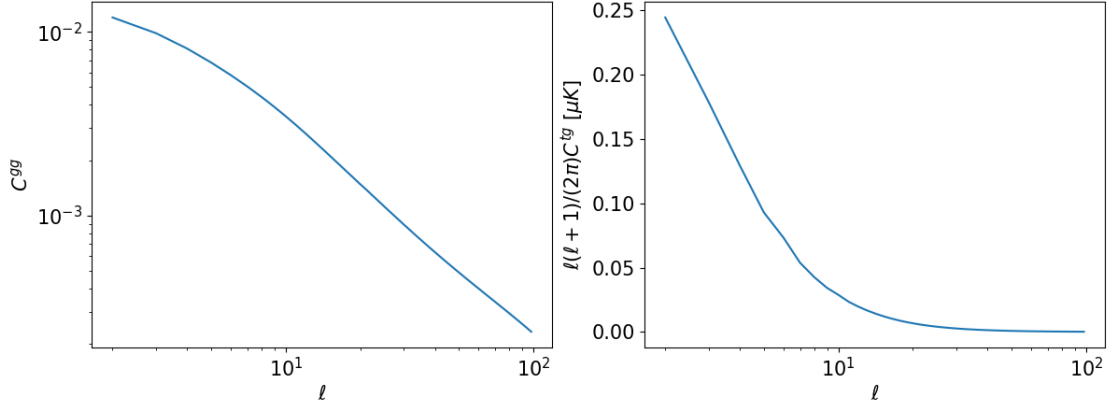
Figure 2.5: Galaxy autocorrelation spectrum (left) and late-ISW contribution to the galaxy-CMB cross-correlation (right). The selection function used to calculate these spectra was parametrized to be compatible with 2MASS' galaxy redshift distribution[16, 39].

The simplest parametrization proposed for dark energy's equation of state is called the Chevallier-Polarski-Linder (CPL) parametrization[26, 44]:

$$w(z) = w_0 + \left(1 - \frac{1}{1+z} \right) w_a. \tag{2.53}$$

So far, this parametrization has not solved some of the current limitations being faced by the ΛCDM model, such as the Hubble tension [48] and the σ_8 tension [6], it has not improved over the ΛCDM predictions, but it shows good compatibility with CMB, type IA supernovae and baryon acoustic oscillations (BAO) data[6]. Planck results using this parametrization are shown in Table 2.2.

Parameter	Marginalized Value
w_0	-0.957 ± 0.080
w_a	$-0.29^{+0.32}_{-0.26}$
$H_0 [\text{km s}^{-1}\text{Mpc}^{-1}]$	68.31 ± 0.82
σ_8	0.820 ± 0.011
$\Delta\chi^2$	-1.4

Table 2.2: Marginalized values and 68% confidence limits for cosmological parameters, assuming parametrization (2.53), obtained by combining Planck temperature and polarization autocorrelation and cross-correlation spectra[49], type IA supernovae data from the Joint Light Curve Analysis (JLA)[50] and BAO data from the Sloan Digital Sky Survey (SDSS)[51]. The $\Delta\chi^2$ value was computed with respect to the ΛCDM best fits computed from the same data set combination.

Another important parameter related to dark energy is its speed of sound, defined as[52]:

$$c_s^2 = \frac{\delta P_{DE}}{\delta \rho_{DE}} \tag{2.54}$$

where ρ_{DE} and P_{DE} are the dark energy's density and pressure respectively, and δ indicates the perturbation of these quantities.

The value of this parameter influences, for instance, the evolution of the gravitational potentials[53], and many other factors that relate to the evolution of the universe, thus having an impact on observables.

Figure 2.6 shows the influence of different parameter values, using the CPL parametrization, on the CMB temperature autocorrelation spectrum, and compares the expected theoretical spectra with Planck's data.

Figure 2.6: The solid lines in the plots correspond to theoretical predictions for the CMB temperature autocorrelation spectra corresponding to different parameter values of the dark energy equation of state, the black data points correspond to Planck's data[6]. Figures 2.6a, 2.6b and 2.6c show how the spectrum changes for a constant value of w_a shown on the top left of the axis and varying speeds of sound, while the other three figures show how the curve behaves with varying values of w_a and a constant speed of sound. All theoretical calculations were done using CAMB.

3 | Optimizing the Selection Function

Equation (2.52) introduced the selection function $\frac{dN}{dz}$, which simply corresponds to the redshift distribution of galaxy counts N and can vary depending on the galaxy catalog used, thus having an influence on the expected cross-correlation and galaxy autocorrelation signals that can be extracted from that catalog. As shown in Figure 2.5, the ISW signal is mostly present at low multipoles, where cosmic variance has a strong influence, making it hard to determine whether the data follow the model or the null hypothesis of zero cross-correlation. This motivated us to study the possibility of optimizing the cross-correlation signal by determining a selection function that could theoretically maximize it, this study will be presented in this chapter.

3.1 Parametrization of the Selection Function

Following [39], we are assuming the selection function can be parametrized as

$$\frac{dN}{dz}\left(z|\lambda, \beta, z_0\right) dz = \frac{\beta}{\Gamma(\lambda)}\left(\frac{z}{z_0}\right)^{\beta\lambda-1}\exp\left[-\left(\frac{z}{z_0}\right)^{\beta}\right] d\left(\frac{z}{z_0}\right) \tag{3.1}$$

where the parameters β, λ and z_0 are all positive. The values used to calculate the spectra in Figure 2.5 are those corresponding to the so called band 1 of the 2MASS infrared galaxy catalog. Table 3.1 shows the parameter values for each band of this catalog, while Figure 3.1 shows the plots for their corresponding selection functions. The details on what each of these bands represent will be presented in chapter 4.

Band	z_0	β	λ
1	0.043	1.825	1.524
2	0.054	1.800	1.600
3	0.067	1.765	1.636
4	0.084	1.723	1.684

Table 3.1: Parameter values for the 4 bands of the 2MASS catalog. Values extracted from [39].

To start the search for an ideal selection function, a good first guess would be to find functions that favor galaxies at redshifts close to the period of transition to the current dark energy dominated universe. The beginning of the period of accelerated expansion can be

Figure 3.1: Selection function calculated for the 4 bands of the 2MASS catalog according to equation (3.1).

estimated by inputing the ΛCDM values for cosmological parameters in the following equation

$$z^* = \left[-(1 + 3w_{DE}) \frac{\Omega_{DE}}{\Omega_m} \right]^{-\frac{1}{3w_{DE}}} - 1, \tag{3.2}$$

which assumes a constant equation of state parameter w_{DE} for dark energy[37]. If we use the values of Table 2.1, we estimate that $z^* \approx 0.63$. By analysing Figure 3.1, it is possible to see that none of the 2MASS bands have peak sensitivity close to this redshift.

To determine the region in the parameter space that favors redshift z^*, a study of the influence of each parameter in the selection function was necessary. Figure 3.2 shows how the selection function varies with changes in each of its parameters.

Figure 3.2 shows that increasing the value of λ seems to shift the peak of the selection function towards higher redshifts without significantly changing the width of the curve, while increasing β seems to narrow the curve without significantly changing the position of the peak, and increasing z_0 seems to increase both the position of the maximum and the width of the curve.

These observations make it easier to change the parameters and see their influence on the cross-correlation signal and helps to choose a region of the parameter space to explore, but to do so, the matter of how to quantify the quality of the signal has to be discussed.
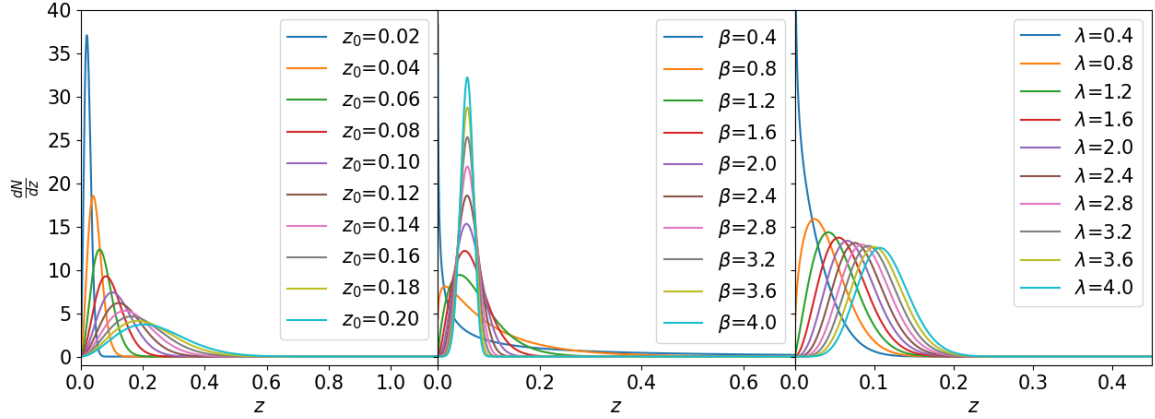
Figure 3.2: Selection function calculated for various parameter values according to the parametrization (3.1). Each plot is made by keeping 2 of its three parameters fixed, corresponding to the band 2 of the 2MASS catalog (see Table 3.1), the corresponding values of the varied parameter can be seen on the legend.

3.2   Maximizing the Cross-Correlation Signal

To maximize the signal we are in search of, we compare it with the null hypothesis, according to which there is no cross-correlation induced by the ISW effect, i.e $C_\ell^{tg} = 0$ for every multipole. One way to do this is to synthesize multiple uncorrelated CMB temperature maps and galaxy contrast maps, calculate the power spectrum C_ℓ^{tg} for each of them and, for each multipole ℓ, determine the distribution of C_ℓ^{tg}, using this as an estimation of the probability distribution of these cross-correlation samples.

In this part of the project, the HEALPix software was used extensively, and to validate the procedure for the search of the probability distribution for the null hypothesis, we first tested how the software would be able to retrieve the signal of a non-null cross-correlation spectrum. To do this, the full autocorrelation spectrum shown in Figure 2.4 calculated using CAMB was used alongside the correlation spectra shown in Figure 2.5 as inputs to *synfast*, a HEALPix harmonic space sampler and harmonic to real space map synthesizer. The synthetic maps generated with this procedure can then be decomposed into spherical harmonics coefficients $a_{\ell m}$ using *anafast*, another HEALPix functionality. Figure 3.3 illustrates one galaxy contrast map and one CMB temperature map synthesized using this procedure.

Figure 3.4 shows a comparison between the theoretical correlation spectra and the ones estimated from averaging the correlation spectra of 10^4 synthetic maps, showing that among the

(a) CMB temperature

(b) Galaxy contrast
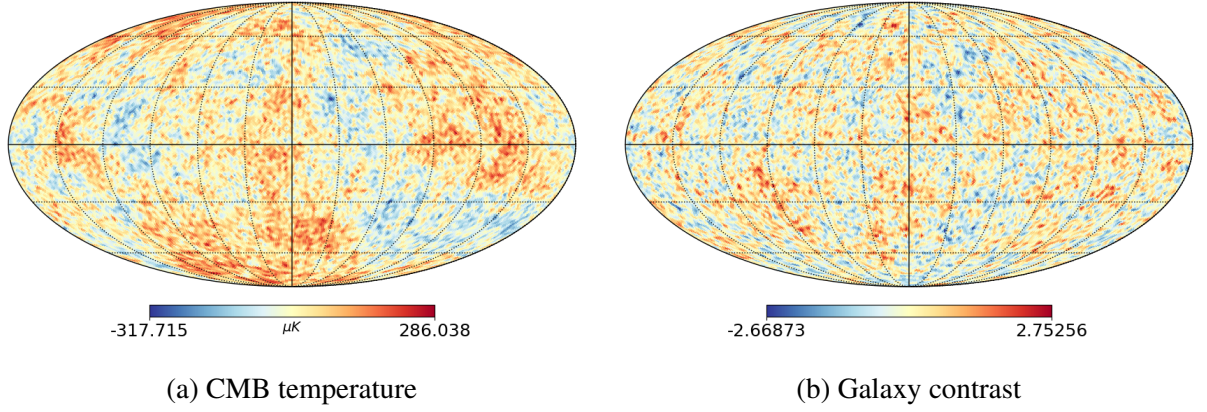
Figure 3.3: Mollweide projection of two instances of maps synthesized using HEALPix with the procedure presented.

three spectra considered here, the cross-correlation is the one most affected by cosmic variance.
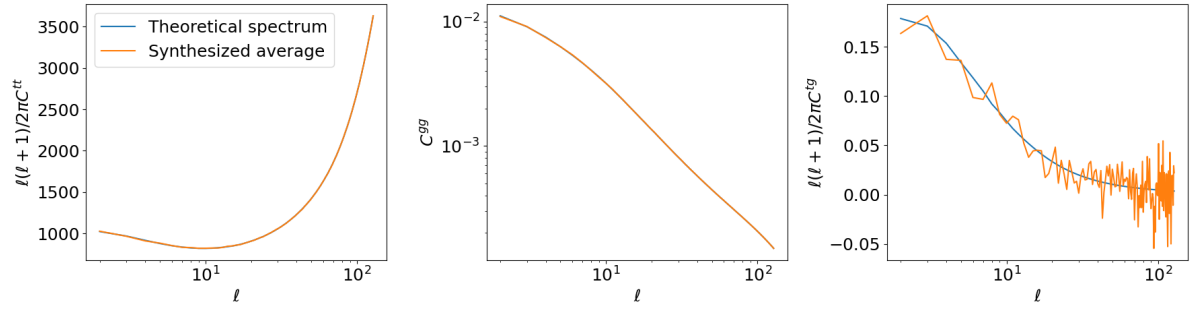
Figure 3.4: Comparison between theoretical auto and cross-correlation spectra and the averages of the C_ℓ calculated from 10^4 synthesized maps using the procedure presented in this section.

In order to determine the probability distribution of the null hypothesis for each multipole, a similar process can be used, but now C^{tg} is set to zero, therefore, the temperature and galaxy contrast maps will be uncorrelated realizations of the autocorrelation spectra C^{tt} and C^{gg}. For each multipole, we have a sample of C_ℓ^{tg}, one value for each map, the distribution of these values can be used as a probability distribution for the null hypothesis at each multipole. Figure 3.5 shows two histograms representing this distribution.

Upon thorough inspection of the histograms, we decided to fit each histogram using Gaussian distributions, which are shown in Figure 3.5, and used the fitted Gaussians as the probability density functions of C_ℓ^{tg} under the null hypothesis. Each of these distributions will be indicated by $f_\ell\left(C_\ell^{tg}\right)$.

With that, we can finally define the probability P_{null} that a correlation spectrum C^{tg} follows

(a) Distribution for $\ell = 4$.　　　　　　(b) Distribution for $\ell = 30$
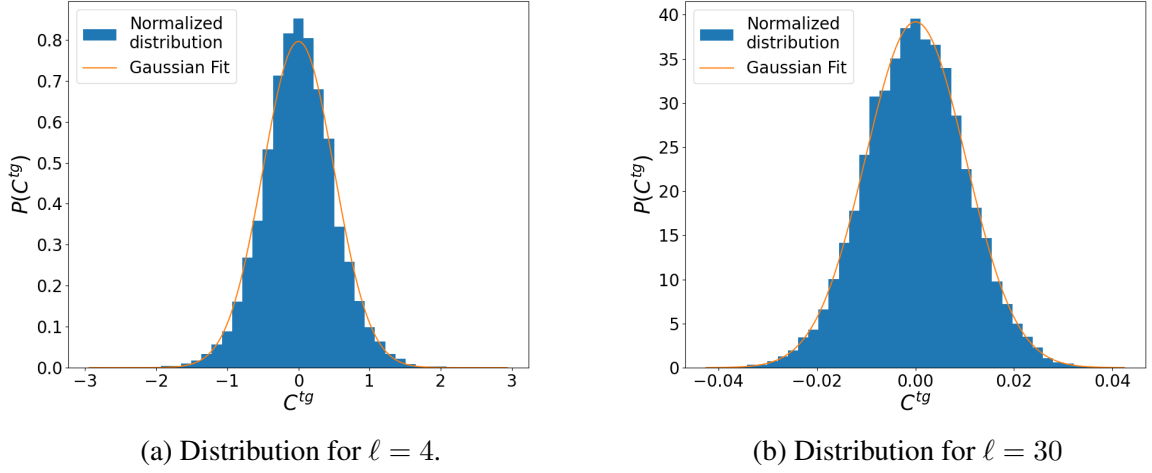
Figure 3.5: Distribution of cross-correlation values on different multipoles for 10^4 maps synthesized with null cross-correlation. Gaussian fits of the samples are shown alnogside the normalized distributions. As expected, the averages of the distributions are close to zero, and the variance of the distribution is significantly higher in low multipoles due to cosmic variance.

the null hypothesis:

$$P_{\text{null}} = \prod_{\ell=2}^{\ell_{\text{max}}} f_\ell \left(C_\ell^{tg} \right) \tag{3.3}$$

We can now explore the parameter space (z_0, β, λ) and look for the values that minimize P_{null}. In other words, for a given cosmological model chosen a priori (in this case ΛCDM) where a CMB-galaxy non-null cross-correlation signal is expected, what is the selection function that minimizes the consistency with a null signal.

To perform an initial exploration of the parameter space for the parametrization (3.1), 2D heat maps were produced by varying 2 of the 3 parameters while maintaining the third parameter fixed, the function mapped was $P_{\text{null}}(z_0, \beta, \lambda)/P_{\text{null}}^{\text{2MASS}}$, where $P_{\text{null}}(z_0, \beta, \lambda)$ is the probability (3.3) calculated using power spectra computed with the selection function that corresponds to the given parameters, and $P_{\text{null}}^{\text{2MASS}}$ is the same probability calculated with the parameters of the band 1 of the 2MASS catalog. Figure 3.6 shows examples of these heat maps.

As shown in Figure 3.6, the region explored does not present a significant reduction in the probability of a certain parameter combination being compatible with the null hypothesis relative to the band 1 of 2MASS, showing no more than a 3% reduction in the ratio. In spite of this, it is possible to see a region of low values for this function where a function minimizer algorithm could possibly be able to start the search for a minimum value.
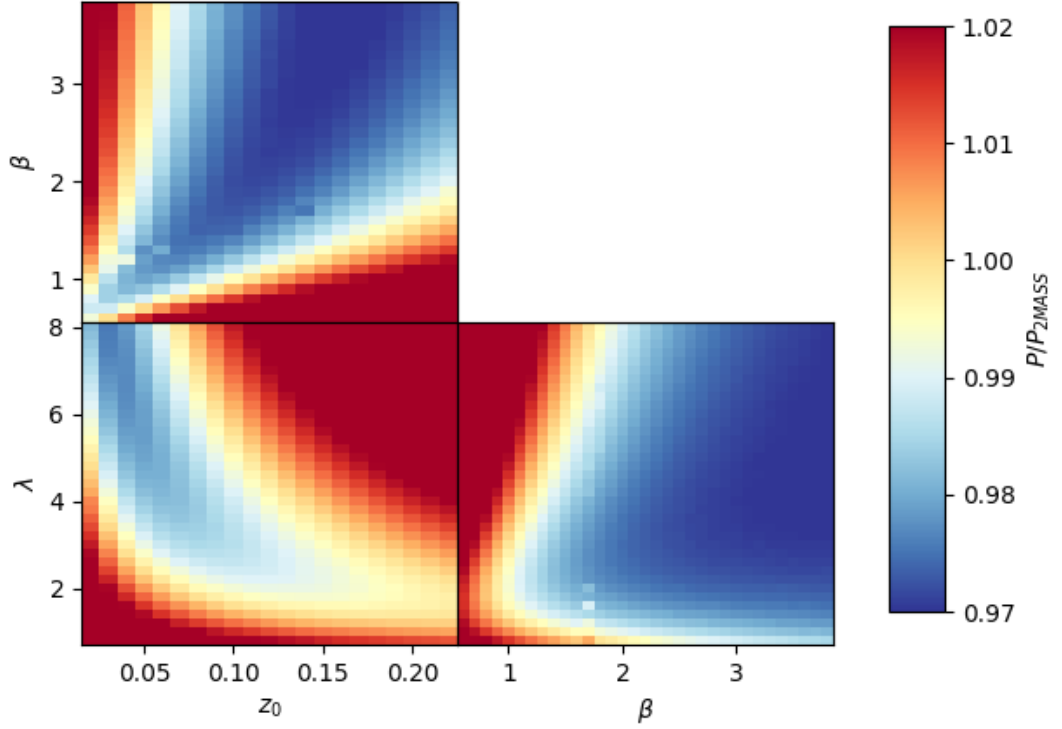
Figure 3.6: For each plot, one parameter is fixed at a certain value. The color of the plot indicates the ratio $P_{\text{null}}(z_0, \beta, \lambda)/P_{\text{null}}^{\text{2MASS}}$, according to the bar on the right. Dark blue regions indicate the lower values of this ratio, these are the regions that improve the signal according to our analysis, and can indicate regions where a minimum value can be found. The constant values are: $\lambda = 5$ (upper left), $\beta = 1$ (lower left) and $z_0 = 0.17$ (lower right).

A code for minimizing the function P_{null} using the GSL library[54] was devised, a few points were used as initial guess to the minimizer, some of them in the dark blue region, and some of them in the light blue regions, to make sure the convergence of the minimizer is reliable, and in every case results were very simillar. The final value used for our analysis was

$$(\beta, z_0, \lambda)_{\text{min}} = (3.088, 0.1508, 4.9401) \tag{3.4}$$

For this combination of parameters, $P_{\text{null}}(z_0, \beta, \lambda)/P_{\text{null}}^{\text{2MASS}} = 0.971$, still a 3% improvement relative to band 1 of 2MASS. Figure 3.7 shows the selection and cross-correlation functions associated to the minimum of equation (3.4).

The selection function shown in Figure 3.7a does not favor the predicted $z^* = 0.63$. This could possibly be reached by increasing the value of λ, but both the minimizer and the heat maps shown in 3.6 indicate that not much statistical value, if any, would be gained from doing

(a) Selection Function   (b) Power Spectra
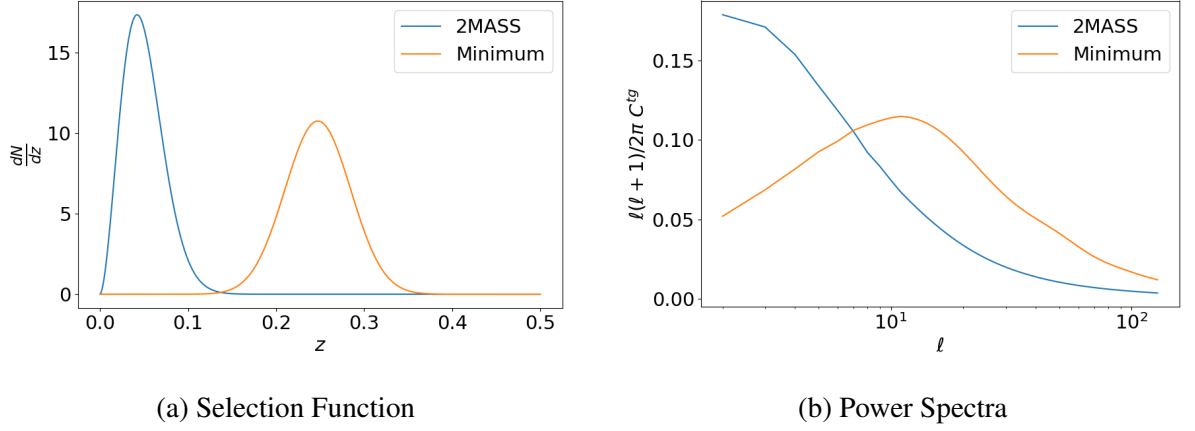
Figure 3.7: Comparison between theoretical properties of the point in parameter space that minimizes the null hypothesis and the band 1 of 2MASS.

so. The power spectra comparison in Figure 3.7b indicates an interesting tradeoff to achieve a better signal: it has a resonably higher signal at around $\ell = 10$, where cosmic variance is not as relevant as it is around $\ell = 2$, but the function has a lower signal at its maximum point.

Despite these insights, the statistical gains from this ideal set of parameters are not very high compared with the 2MASS signal if we assume our galaxy catalog follows the parametrization (3.1) and that dark energy has a constant equation of state.

4 | Extracting Correlations from Data

CMB experiments do not directly measure correlation spectra, instead the data consists of time ordered data streams, each stream with information of the direction of observation and the sky temperature measured by that detector, which is contained within an array of detectors.

In this chapter, the process of converting this signal, taking into account the effects of detector noise and environmental variables such as the galactic background, will be discussed, not only for CMB but also for galaxy maps. A Monte Carlo Markov Chain (MCMC) algorithm capable of efficiently extracting these correlations, including the galaxy-CMB cross-correlation, will be presented.

4.1   Two Point Functions

To estimate any correlation spectrum, we first need to estimate the values of the multipole terms $a_{\ell m}$, but applying equation (2.43) to these directly does not yield accurate results, one has to introduce factors such as noise and map masks first.

In general, it is common to introduce a weight function $W(\hat{\mathbf{n}})$ to account for various possible effects on the measured maps, such as galactic contamination, edge effects, and down-weighting more noisy pixels[55]. If we ignore other effects for now (such as noise), the multipole terms $\tilde{a}_{\ell m}$ as defined in (2.42), assuming a high number of small pixels to approximate a sum with an integral, becomes

$$\tilde{a}_{\ell m} = \int d\Omega \Theta(\hat{\mathbf{n}}) W(\hat{\mathbf{n}}) Y_{\ell m}^*(\hat{\mathbf{n}}). \tag{4.1}$$

With this, one can define the so-called pseudo-power spectrum $\tilde{C}_\ell$:

$$\tilde{C}_\ell = \frac{1}{2\ell + 1} \sum_{m=-\ell}^{\ell} |\tilde{a}_{\ell m}|^2. \tag{4.2}$$

Still ignoring noise and other factors, one can relate the ensemble average of the pseudo-power spectrum with the true power spectrum with a simple system of equations

$$\left\langle \tilde{C}_\ell \right\rangle = \sum_{\ell'} M_{\ell\ell'} \left\langle C_\ell \right\rangle, \tag{4.3}$$

where $M_{\ell\ell'}$ is a matrix that describes the coupling between modes, called the multipole mixing matrix. If the mask applied to a CMB map is described by multipole functions $\mathcal{W}_\ell$, the mixing matrix corresponds to

$$M_{\ell\ell'} = \frac{2\ell'+1}{4\pi} \sum_{\ell''} (2\ell''+1)\mathcal{W}''_\ell \begin{pmatrix} \ell & \ell' & \ell'' \\ 0 & 0 & 0 \end{pmatrix}^2, \tag{4.4}$$

in which the term in parenthesis is a Wigner-$3j$ symbol.

To determine the full form of the system of equations used to determine the real power spectrum, one has to take noise into consideration the so-called beam pattern.

In radio astronomy, telescopes take measurements in various angles in the sky, and for each direction $\hat{n}$, there is an area of the sky being covered by the measurement, each of these areas is called a beam. In an apparatus that measures CMB photons' temperatures, the measurement in each direction $\hat{n}$ is a temperature $T^{\text{obs}}(\hat{n})$, this measurement corresponds to a weighted combination of the real temperatures $T(\hat{n}')$ over the beam plus a noise $\eta(\hat{n})$:

$$T^{\text{obs}}(\hat{n}) = \int_{\text{beam}} d\Omega B(\hat{n}, \hat{n}')T(\hat{n}') + \eta(\hat{n}). \tag{4.5}$$

The function $B(\hat{n}, \hat{n}')$ is called the beam pattern, it weights the contributions of photons coming in the directions around the beam, and it can be estimated during the calibration of the apparatus, it is usually assumed to be Gaussian. Figure 4.1 shows the beam pattern for the Planck instrument at 30 GHz.

With the multipole terms B_ℓ of the beam pattern $B(\hat{n}, \hat{n}')$, and given a noise map N that can also be expanded in multipoles N_ℓ, the correlation functions can be extracted by solving the following system of equations:

$$\left\langle \tilde{C}_\ell \right\rangle = \sum_{\ell'} M_{\ell\ell'} B_{\ell'}^2 \left\langle C_{\ell'} \right\rangle + \left\langle N_\ell \right\rangle. \tag{4.6}$$

Although this solution converges to the true power spectrum in the limit of a large number of sky realizations, having a single universe to retrieve sky map multipoles makes this solution
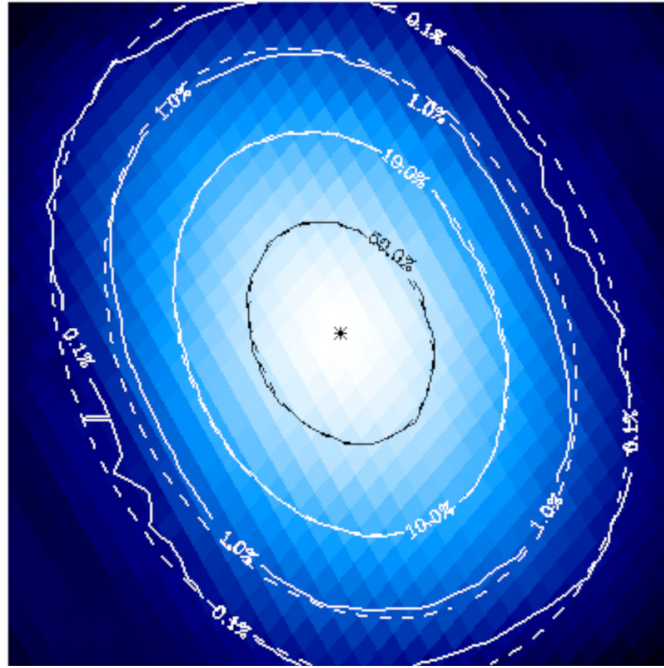
Figure 4.1: Beam pattern for the Planck instrument at 30 GHz. Contours delineate the regions where the beam function drops from its maximum to 50%, 10%, 1% and 0.1% respectively. Source: Planck wiki.

highly affected by cosmic variance[16]. Another limitation of this method is its computational complexity of $O(N_p^3)$, where N_p is the number of pixels of the sample maps. For experiments such as WMAP ($N_p \sim 10^6$) and Planck ($N_p \sim 10^7$), this time complexity becomes computationally unviable, thus motivating the introduction of a new technique, which will be presented now.

4.2   Gibbs Sampling

For a more efficient method than the one presented previously, Monte Carlo (MC) methods to sample maps of the primordial signal from the a posteriori probability distribution taking into account cosmic variance, instrumental noise, and residual foregrounds were developed[56–58].

Let d be a pixelized temperature map consisting of primordial signal $\mathbf{s}$ and instrumental noise $\mathbf{n}$, both following Gaussian distributions with covariance matrices $\mathbf{S}$ and $\mathbf{N}$ respectively, with a full covariance matrix $\mathbf{C} = \mathbf{S} + \mathbf{N}$. The likelihood for observing such a map, after marginalizing over the unknown signal $\mathbf{s}$, can be calculated using

$$\mathcal{L} = P(\mathbf{d}|\mathbf{C}) = \frac{1}{(2\pi)^{n_{\text{dim}}/2}|\mathbf{C}|^{1/2}}\exp\left(-\frac{1}{2}\mathbf{d}^T\mathbf{C}^{-1}\mathbf{d}\right), \tag{4.7}$$

where $n_{\text{dim}} = N_p^2$. The direct evaluation of this likelihood is not computationally viable due to the calculation of the determinant of $\mathbf{C}$, a matrix that cannot be represented in diagonal form, since $\mathbf{N}$ is typically close to diagonal in pixel space and S is diagonal in harmonic space.

Using Bayes' theorem, this likelihood can be written as $P(\mathbf{C}|\mathbf{d}) \propto \pi(\mathbf{S})P(\mathbf{d}|\mathbf{C})$, where $\pi(\mathbf{S})$ is the prior on the power spectrum and $P(\mathbf{C}|\mathbf{d})$ is the posterior probability density.

The calculation $P(\mathbf{C}|\mathbf{d})$ can be done using an MC method called Gibbs sampling. Suppose we can sample from the conditional probabilities $P(\mathbf{C}|\mathbf{s},\mathbf{d})$ and $P(\mathbf{s}|\mathbf{C},\mathbf{d})$, we can then sample a set of $\{(\mathbf{s}^i, \mathbf{C}^i)\}$ by iterating the following sampling process[59]:

$$\mathbf{s}^{i+1} \leftarrow P(\mathbf{s}|\mathbf{C}^i, \mathbf{d}), \tag{4.8}$$

$$\mathbf{C}^{i+1} \leftarrow P(\mathbf{C}|\mathbf{s}^{i+1}, \mathbf{d}). \tag{4.9}$$

From this sample, one can use the so called Blackwell-Rao estimator to determine an approximation for $P(\mathbf{C}|\mathbf{d})$[59]. To construct this estimator, we first expand each element of the vector $\mathbf{s}$ in terms of spherical harmonics:

$$\mathbf{s}(\theta, \phi) = \sum_{\ell=0}^{\infty}\sum_{m=-\ell}^{\ell} \mathbf{s}_{\ell m}Y_{\ell m}(\theta, \phi), \tag{4.10}$$

and define

$$\sigma_\ell = \frac{1}{2\ell+1}\sum_{m=-\ell}^{\ell}\mathbf{s}_{\ell m}\mathbf{s}_{\ell m}^\dagger. \tag{4.11}$$

With this, it is possible to derive the Blackwell-Rao estimator for the density $P(C_\ell|\mathbf{d})$:

$$P(C_\ell|\mathbf{d}) \approx \frac{1}{N_G}\sum_{i=1}^{N_G} P(C_\ell|\sigma_\ell^i), \tag{4.12}$$

where N_G is the number of Gibbs samples and C_ℓ are the multipole values due to the true signal $\mathbf{s}$.

In this project, the same process presented in [16], which is an extended version of what is presented in [60], has been used. In this framework, the vector $\mathbf{s}$ and the matrix $\mathbf{S}$ are defined as

$$\mathbf{s}^T = (s^{tg}_{00}, s^{tg}_{01}, s^{tg}_{11}, \ldots, s^{tg}_{\ell_{\max}0}, \ldots, s^{tg}_{\ell_{\max}\ell_{\max}}),\qquad(4.13)$$

$$\mathbf{S} = \mathrm{diag}(S^{tg}_0, S^{tg}_1, S^{tg}_1, \ldots, S^{tg}_{\ell_{\max}}, \ldots, S^{tg}_{\ell_{\max}}),\qquad(4.14)$$

where

$$\mathbf{s}^{tg}_{\ell m} = \begin{pmatrix} a^t_{\ell m} \\ a^g_{\ell m} \end{pmatrix}, \qquad\qquad \mathbf{S}^{tg}_\ell = \begin{pmatrix} C^{tt}_\ell & C^{tg}_\ell \\ C^{tg}_\ell & C^{gg}_\ell \end{pmatrix}.\qquad(4.15)$$

It is also assumed that the noise covariance is diagonal: $N = \mathrm{diag}(N^{tg}_{11}, \ldots, N^{tg}_{ii}, \ldots, N^{tg}_{pp})$ where

$$N^{tg}_{ii} = \begin{pmatrix} N^{tt}_{ii} & 0 \\ 0 & N^{gg}_{ii} \end{pmatrix},\qquad(4.16)$$

since the noises affecting the temperature anisotropies and galaxy contrast are uncorrelated.

4.3   Data Sets and Analysis

In this project, we have used two main datasets for our analysis: CMB data from the Wilkinson Microwave Anisotropy Probe (WMAP)[5, 61] and galaxy contrast data from the Two Micron All Sky Survey (2MASS) catalog[62]. In this section, the details about these data sets and their respective analysis pipelines will be explored.

4.3.1   2MASS Catalog

From 1997 to 2001, the 2MASS collected raw imaging data covering 99.998% of the celestial sphere in three near-infrared bands: J ($1.25\,\mu$m), H ($1.65\,\mu$m) and K_s ($2.16\,\mu$m). This produced a Point Source Catalog containing more than 4.7×10^8 point sources and an Extended Source Catalog (XSC) of $1,647,599$ extended sources, which is the catalog we will use in this project to trace the galaxy contrast in the sky. This catalog contains sources that are extended with respect to instanteneous point source functions (PSF), such as galaxies and galactic nebulae.

The K_s band's 20 mag arcsec^{-2} isophotal circular aperture magnitudes (here simply called

K_{20}) were corrected for galactic extinction using the reddening maps $E(B - V)$ at $100\,\mu\text{m}$ in [63], according to the expression $K_{20} \to K'_{20} = K_{20} - A_k$, where $A_k = 0.367E(B - V)$.

HEALPix was used to produce and analyse the maps with resolution parameter $nside = 32$, a mask was applied to every pixel with $A_k > 0.05$. This left the catalog at $801,476$ objects with $12 < K'_{20} < 14$, which were further divided into the four bands: Bands 1 ($12.0 < K'_{20} < 12.5$), 2 ($12.5 < K'_{20} < 13.0$), 3 ($13.0 < K'_{20} < 13.5$) and 4 ($13.5 < K'_{20} < 14.0$).

This catalog is made using photometric measurements, meaning redshift information is not directly obtained with the measurements, but there are techniques to estimate photometric redshifts. In [64] the luminosity function of 4192 2MASS galaxies were used to estimate the luminosity function of the entirety of the K_s band, and then the photometric redshifts of these galaxies. In [65] the authors trained a neural network and cross-correlated XSC with WISE[66] and SuperCOSMOS[67] to obtain the photometric redshifts of a big fraction of the sources in XSC, creating what is called the 2MPZ catalog. As shown in [16], using the 2MPZ catalog over XSC does not yield significant changes in the results, so in this project we maintained the usage of the XSC data.

As explained in section 3.1, the redshift distribution of galaxy counts can be parametrized using the selection function defined in equation (3.1), the parametrizations for each band is shown in Table 3.1 and the plots of these selection functions is shown in Figure 3.1. Figure ?? shows the final maps produced after this process.

IMAGENS DOS MAPAS COM MÁSCARA

4.3.2 WMAP Data

WMAP used radiometers and differential microwave receivers to measure the CMB temperature over the entire sky across five frequency bands in the spectral region where the CMB-to-foreground ratio is near its maximum[61]. Out of these 5 frequency bands, we have used in this project the data corresponding to the Q (40GHz), V (60GHz) and W (90GHz) bands, which are the ones suitable for data analysis. Its last data realease, WMAP9, which is the one used in this project, contains high resolution temperature intensity maps with noise power that can be well modeled as uncorrelated Gaussian fluctuations with variances given by $\sigma_0^2/N_{\text{obs}}$, where σ_0 is a parameter present in the data for each channel.

Figure ?? shows the maps used for the analysis with the so called KQ85 mask applied to

them.

IMAGENS DOS MAPAS WMAP

5 | Results

6 | Conclusions

Artigo do Edivaldo: [16]

ISW artigo original: [15]

The GNU parallel software was used: [68]

Cobaya: [69, 70]

Gibbs Sampling: [71]

Appendices

A | Demonstration of Correlation Functions

Expanding the definition of C_ℓ^{TT} given in (2.43) one can show that[23]:

$$C_\ell^{tt} = \frac{2}{\pi} \int dk k^2 P(k) \left| \frac{\Theta_\ell(k, \eta_0)}{\delta(k, \eta_0)} \right|^2.$$
(A.1)

Similar expressions can be found for C_ℓ^{tg} and C_ℓ^{gg}, we will focus the demonstration on the temperature autocorrelation case.

Using the ISW term of equation (2.45)

$$\Theta_\ell^{\text{ISW}}(k, \eta_0) = \int_0^{\eta_0} d\eta e^{-\tau} [\Psi'(k, \eta) - \Phi'(k, \eta)] j_\ell[k(\eta_0 - \eta)],$$
(A.2)

with $e^{-\tau} \approx 1$ since, as shown, the ISW effect is only relevant at small scales[1]. So

$$\Theta_\ell^{\text{ISW}}(k, \eta_0) = \int_0^{\eta_0} d\eta \frac{\mathrm{d}}{\mathrm{d}\eta} \left[\Psi(k, \eta) - \Phi(k, \eta) \right] j_\ell[k(\eta_0 - \eta)],$$
(A.3)

Using the definition of η in (2.46)

$$\eta = \int_0^t \frac{dt}{a(t)} = \int_0^a \frac{da'}{a'^2 H(a')} = \int_z^\infty \frac{dz'}{H(z)},$$
(A.4)

we can do a change in variables of the integral to redshift. Since

$$\eta_0 - \eta = \int_0^\infty \frac{dz'}{H(z')} - \int_z^\infty \frac{dz'}{H(z')} = \int_z^\infty \frac{dz'}{H(z')} = \chi(z),$$
(A.5)

where $\chi(z)$ is the comoving distance, equation (A.3) becomes

$$\Theta_\ell^{\text{ISW}}(k, z = 0) = \int_0^\infty dz \frac{\mathrm{d}}{\mathrm{d}z} \left[\Psi(k, z) - \Phi(k, z) \right] j_\ell[k\chi(z)].$$
(A.6)

At late times, we can neglect anisotropic stress, taking $\Psi \approx \Phi$, therefore

$$\Theta_\ell^{\text{ISW}}(k, 0) = -2 \int_0^\infty dz \frac{\mathrm{d}\Phi}{\mathrm{d}z} j_\ell[k\chi(z)].$$
(A.7)

Finally, we can use the Poisson equation

---

[1]The Planck best-fit for the optical depth in the present is $\tau = 0.054 \pm 0.007$

$$\Phi(k, z) = \frac{3}{2}\Omega_m \left(\frac{H_0}{k}\right)^2 (1+z)\delta(k, z), \tag{A.8}$$

to show that

$$\delta(k, 0) = \frac{2}{3\Omega_m} \left(\frac{k}{H_0}\right)^2 \Phi(k, 0). \tag{A.9}$$

With this:

$$\frac{\Theta_\ell(k, \eta_0)}{\delta(k, \eta_0)} = \frac{\Theta_\ell(k, z=0)}{\delta(k, z=0)} = -3\Omega_m \left(\frac{H_0}{k}\right)^2 \int_0^\infty dz \frac{\mathrm{d}}{\mathrm{d}z} \left[\frac{\Phi(k, z)}{\Phi(k, 0)}\right] j_\ell[k\chi(z)]. \tag{A.10}$$

Cosmologists define the growth function $D(z)$ as

$$\frac{\Phi(k, a)}{\Phi(k, 1)} \equiv \frac{D(a)}{a} = (1+z)D(z) = \frac{\Phi(k, z)}{\Phi(k, 0)}, \tag{A.11}$$

so

$$\frac{\Theta_\ell(k, \eta_0)}{\delta(k, \eta_0)} = -3\Omega_m \left(\frac{H_0}{k}\right)^2 \int_0^\infty \frac{\mathrm{d}(1+z)D(z)}{\mathrm{d}z} j_\ell[k\chi(z)]. \tag{A.12}$$

Using this result, equation (A.1) in terms of redshift instead of η becomes

$$C_\ell^{tt} = \frac{2}{\pi} \int_0^\infty dk k^2 P(k)|W_\ell^t|^2 \tag{A.13}$$

with

$$W_\ell^t = -3\Omega_m \left(\frac{H_0}{k}\right)^2 \int_0^\infty \frac{\mathrm{d}(1+z)D(z)}{\mathrm{d}z} j_\ell[k\chi(z)]. \tag{A.14}$$

Equation (A.3) expresses the present contribution of the late ISW effect to the CMB temperature autocorrelation spectrum.

Bibliography

[1] A. A. Penzias and R. W. Wilson. "A Measurement of Excess Antenna Temperature at 4080 Mc/s." In: *Astrophysical Journal* 142 (July 1965), pp. 419–421. DOI: `10.1086/148307`.

[2] Ivan Agullo, Dimitrios Kranas, and V Sreenath. "Large scale anomalies in the CMB and non-Gaussianity in bouncing cosmologies". In: *Classical and Quantum Gravity* 38.6 (Feb. 2021), p. 065010. DOI: `10.1088/1361-6382/abc521`. URL: `https://dx.doi.org/10.1088/1361-6382/abc521`.

[3] Xingang Chen. "Primordial Non-Gaussianities from Inflation Models". In: *Adv. Astron.* 2010 (2010), p. 638979. DOI: `10.1155/2010/638979`. arXiv: `1002.1416 [astro-ph.CO]`.

[4] Robert G. Crittenden and Neil Turok. "Looking for a Cosmological Constant with the Rees-Sciama Effect". In: *Phys. Rev. Lett.* 76 (4 Jan. 1996), pp. 575–578. DOI: `10.1103/PhysRevLett.76.575`. URL: `https://link.aps.org/doi/10.1103/PhysRevLett.76.575`.

[5] G. Hinshaw et al. "FIVE-YEAR WILKINSON MICROWAVE ANISOTROPY PROBE* OBSERVATIONS: DATA PROCESSING, SKY MAPS, AND BASIC RESULTS". In: *The Astrophysical Journal Supplement Series* 180.2 (Feb. 2009), p. 225. DOI: `10.1088/0067-0049/180/2/225`. URL: `https://dx.doi.org/10.1088/0067-0049/180/2/225`.

[6] Planck Collaboration et al. "Planck 2018 results - VI. Cosmological parameters (Corrigendum)". In: *Astronomy & Astrophysics* 652 (2021), p. C4. DOI: `10.1051/0004-6361/201833910e`. URL: `https://doi.org/10.1051/0004-6361/201833910e`.

[7] P. J. E. Peebles and J. T. Yu. "Primeval adiabatic perturbation in an expanding universe". In: *Astrophys. J.* 162 (1970), pp. 815–836. DOI: `10.1086/150713`.

[8] D. J. Fixsen. "THE TEMPERATURE OF THE COSMIC MICROWAVE BACKGROUND". In: *The Astrophysical Journal* 707.2 (Nov. 2009), p. 916. DOI: `10.1088/0004-637X/707/2/916`. URL: `https://dx.doi.org/10.1088/0004-637X/707/2/916`.

[9] Wayne Hu and Naoshi Sugiyama. "Anisotropies in the Cosmic Microwave Background: an Analytic Approach". In: *The Astrophysical Journal* 444 (May 1995), p. 489. DOI: `10.1086/175624`. arXiv: `astro-ph/9407093 [astro-ph]`.

[10] D. J. Fixsen et al. "Calibration of the COBE FIRAS Instrument". In: *The Astrophysical Journal* 420 (Jan. 1994), p. 457. DOI: `10.1086/173577`.

[11] Marc Kamionkowski, Arthur Kosowsky, and Albert Stebbins. "A Probe of Primordial Gravity Waves and Vorticity". In: *Phys. Rev. Lett.* 78 (11 Mar. 1997), pp. 2058–2061. DOI: `10.1103/PhysRevLett.78.2058`. URL: `https://link.aps.org/doi/10.1103/PhysRevLett.78.2058`.

[12]   Silvia Galli et al. "CMB polarization can constrain cosmology better than CMB tem-
       perature". In: *Phys. Rev. D* 90 (6 Sept. 2014), p. 063504. DOI: `10.1103/PhysRevD.`
       `90.063504`. URL: `https://link.aps.org/doi/10.1103/PhysRevD.90.`
       `063504`.

[13]   P. A. R. Ade et al. "Improved Constraints on Primordial Gravitational Waves using
       Planck, WMAP, and BICEP/Keck Observations through the 2018 Observing Season". In:
       Phys. Rev. Lett. 127 (15 Oct. 2021), p. 151301. DOI: `10.1103/PhysRevLett.127.`
       `151301`. URL: `https://link.aps.org/doi/10.1103/PhysRevLett.127.`
       `151301`.

[14]   The Planck Collaboration. *The Scientific Programme of Planck.* 2006. arXiv: `astro-`
       `ph/0604069 [astro-ph]`.

[15]   R. K. Sachs and A. M. Wolfe. "Perturbations of a cosmological model and angular
       variations of the microwave background". In: *Astrophys. J.* 147 (1967), pp. 73–90. DOI:
       `10.1007/s10714-007-0448-9`.

[16]   E. Moura-Santos et al. "A Bayesian Estimate of the CMB–large-scale Structure Cross-
       correlation". In: *The Astrophysical Journal* 826.2 (July 2016), p. 121. DOI: `10.3847/`
       `0004-637X/826/2/121`. URL: `https://dx.doi.org/10.3847/0004-`
       `637X/826/2/121`.

[17]   Albert Einstein. "Cosmological Considerations in the General Theory of Relativity". In:
       Sitzungsber. Preuss. Akad. Wiss. Berlin (Math. Phys.) 1917 (1917), pp. 142–152.

[18]   Y. Choquet-Bruhat. *General Relativity and the Einstein Equations.* Oxford Mathematical
       Monographs. OUP Oxford, 2008. ISBN: 9780191578854. URL: `https://books.`
       `google.com.br/books?id=UjHbm5rfpi8C`.

[19]   Suman Sarkar, Biswajit Pandey, and Rishi Khatri. "Testing isotropy in the Universe
       using photometric and spectroscopic data from the SDSS". In: *Monthly Notices of the
       Royal Astronomical Society* 483.2 (Nov. 2018), pp. 2453–2464. ISSN: 0035-8711. DOI:
       `10.1093/mnras/sty3272`. eprint: `https://academic.oup.com/mnras/`
       `article-pdf/483/2/2453/27184728/sty3272.pdf`. URL: `https://doi.`
       `org/10.1093/mnras/sty3272`.

[20]   Biswajit Pandey and Suman Sarkar. "Testing homogeneity of the galaxy distribution in
       the SDSS using Renyi entropy". In: *Journal of Cosmology and Astroparticle Physics*
       2021.07 (July 2021), p. 019. DOI: `10.1088/1475-7516/2021/07/019`. URL:
       `https://dx.doi.org/10.1088/1475-7516/2021/07/019`.

[21]   Edwin Hubble. "A Relation between Distance and Radial Velocity among Extra-Galactic
       Nebulae". In: *Proceedings of the National Academy of Science* 15.3 (Mar. 1929), pp. 168–
       173. DOI: `10.1073/pnas.15.3.168`.

[22]   Georges Lemaitre. "A Homogeneous Universe of Constant Mass and Growing Radius
       Accounting for the Radial Velocity of Extragalactic Nebulae". In: *Annales Soc. Sci.
       Bruxelles A* 47 (1927), pp. 49–59. DOI: `10.1007/s10714-013-1548-3`.

[23]   S. Dodelson and F. Schmidt. *Modern Cosmology.* Elsevier Science, 2020. ISBN: 9780128159484.
       URL: `https://books.google.com.br/books?id=GGjfywEACAAJ`.

[24] Fulvio Melia. "The Friedmann–Lemaître–Robertson–Walker metric". In: *Modern Physics Letters A* 37.03 (2022), p. 2250016. DOI: `10.1142/S021773232250016X`. eprint: `https://doi.org/10.1142/S021773232250016X`. URL: `https://doi.org/10.1142/S021773232250016X`.

[25] Steven Weinberg. "The cosmological constant problem". In: *Rev. Mod. Phys.* 61 (1 Jan. 1989), pp. 1–23. DOI: `10.1103/RevModPhys.61.1`. URL: `https://link.aps.org/doi/10.1103/RevModPhys.61.1`.

[26] Verónica Motta et al. "Taxonomy of Dark Energy Models". In: *Universe* 7.6 (2021), p. 163. DOI: `10.3390/universe7060163`. arXiv: `2104.04642 [astro-ph.CO]`.

[27] B. Schutz. *A First Course in General Relativity*. Cambridge University Press, 2009. ISBN: 9780521887052.

[28] Ofer Lahav and Andrew R Liddle. *The Cosmological Parameters 2014*. 2014. arXiv: `1401.1389 [astro-ph.CO]`.

[29] Alan H. Guth. "Inflationary universe: A possible solution to the horizon and flatness problems". In: *Phys. Rev. D* 23 (2 Jan. 1981), pp. 347–356. DOI: `10.1103/PhysRevD.23.347`. URL: `https://link.aps.org/doi/10.1103/PhysRevD.23.347`.

[30] A.D. Linde. "A new inflationary universe scenario: A possible solution of the horizon, flatness, homogeneity, isotropy and primordial monopole problems". In: *Physics Letters B* 108.6 (1982), pp. 389–393. ISSN: 0370-2693. DOI: `https://doi.org/10.1016/0370-2693(82)91219-9`. URL: `https://www.sciencedirect.com/science/article/pii/0370269382912199`.

[31] Antony Lewis, Anthony Challinor, and Anthony Lasenby. "Efficient computation of CMB anisotropies in closed FRW models". In: *ApJ* 538 (2000), pp. 473–476. DOI: `10.1086/309179`. arXiv: `astro-ph/9911177 [astro-ph]`.

[32] Antony Lewis and Sarah Bridle. "Cosmological parameters from CMB and other data: A Monte Carlo approach". In: *PRD* 66 (2002), p. 103511. DOI: `10.1103/PhysRevD.66.103511`. arXiv: `astro-ph/0205436 [astro-ph]`.

[33] D. J. Fixsen et al. "Calibration of the COBE FIRAS Instrument". In: *The Astrophysical Journal* 420 (Jan. 1994), p. 457. DOI: `10.1086/173577`.

[34] Planck Collaboration et al. "Planck 2013 results. XXVII. Doppler boosting of the CMB: Eppur si muove". In: *Astronomy & Astrophysics* 571 (2014), A27. DOI: `10.1051/0004-6361/201321556`. URL: `https://doi.org/10.1051/0004-6361/201321556`.

[35] Esteban Ricardo Chalbaud Mogollón. *Kinematic effects and the break of statistical isotropy of the cosmic microwave background fluctuations*. 2021. DOI: `https://doi.org/10.11606/D.43.2021.tde-31052021-162009`.

[36] K. M. Górski et al. "HEALPix: A Framework for High-Resolution Discretization and Fast Analysis of Data Distributed on the Sphere". In: *ApJ* 622 (Apr. 2005), pp. 759–771. DOI: `10.1086/427976`. eprint: `astro-ph/0409513`.

[37] José Carlos N. de Araujo. "The dark energy–dominated Universe". In: *Astroparticle Physics* 23.2 (2005), pp. 279–286. ISSN: 0927-6505. DOI: `https://doi.org/10.1016/j.astropartphys.2004.12.004`. URL: `https://www.sciencedirect.com/science/article/pii/S0927650504002087`.

[38] Robert G. Crittenden and Neil Turok. "Looking for a Cosmological Constant with the Rees-Sciama Effect". In: *Phys. Rev. Lett.* 76 (4 Jan. 1996), pp. 575–578. DOI: `10.1103/PhysRevLett.76.575`. URL: `https://link.aps.org/doi/10.1103/PhysRevLett.76.575`.

[39] Niayesh Afshordi, Yeong-Shang Loh, and Michael A. Strauss. "Cross-correlation of the cosmic microwave background with the 2MASS galaxy survey: Signatures of dark energy, hot gas, and point sources". In: *Phys. Rev. D* 69 (8 Apr. 2004), p. 083524. DOI: `10.1103/PhysRevD.69.083524`. URL: `https://link.aps.org/doi/10.1103/PhysRevD.69.083524`.

[40] S. P. Boughn and R. G. Crittenden. "The cross-correlation between the microwave and X-ray backgrounds: foregrounds and systematics". In: *Monthly Notices of the Royal Astronomical Society* 360.3 (July 2005), pp. 1013–1021. ISSN: 0035-8711. DOI: `10.1111/j.1365-2966.2005.09090.x`. eprint: `https://academic.oup.com/mnras/article-pdf/360/3/1013/3178164/360-3-1013.pdf`. URL: `https://doi.org/10.1111/j.1365-2966.2005.09090.x`.

[41] S.P. Boughn and R.G. Crittenden. "A detection of the integrated Sachs–Wolfe effect". In: *New Astronomy Reviews* 49.2 (2005). Sources and Detection of Dark Matter and Dark Energy in the Universe, pp. 75–78. ISSN: 1387-6473. DOI: `https://doi.org/10.1016/j.newar.2005.01.005`. URL: `https://www.sciencedirect.com/science/article/pii/S1387647305000096`.

[42] Planck Collaboration et al. "Planck 2015 results - XXI. The integrated Sachs-Wolfe effect". In: *A&A* 594 (2016), A21. DOI: `10.1051/0004-6361/201525831`. URL: `https://doi.org/10.1051/0004-6361/201525831`.

[43] A J Mead et al. "hmcode-2020: improved modelling of non-linear cosmological power spectra with baryonic feedback". In: *Monthly Notices of the Royal Astronomical Society* 502.1 (Jan. 2021), pp. 1401–1422. ISSN: 0035-8711. DOI: `10.1093/mnras/stab082`. eprint: `https://academic.oup.com/mnras/article-pdf/502/1/1401/42438464/stab082.pdf`. URL: `https://doi.org/10.1093/mnras/stab082`.

[44] Eric V. Linder. "Exploring the Expansion History of the Universe". In: *Phys. Rev. Lett.* 90 (9 Mar. 2003), p. 091301. DOI: `10.1103/PhysRevLett.90.091301`. URL: `https://link.aps.org/doi/10.1103/PhysRevLett.90.091301`.

[45] Chao-Jun Feng et al. "A new class of parametrization for dark energy without divergence". In: *Journal of Cosmology and Astroparticle Physics* 2012.09 (Sept. 2012), p. 023. DOI: `10.1088/1475-7516/2012/09/023`. URL: `https://dx.doi.org/10.1088/1475-7516/2012/09/023`.

[46] A. Hernández-Almada et al. "Stability analysis and constraints on interacting viscous cosmology". In: *Phys. Rev. D* 101 (6 Mar. 2020), p. 063516. DOI: `10.1103/PhysRevD.101.063516`. URL: `https://link.aps.org/doi/10.1103/PhysRevD.101.063516`.

[47] A. Amariti et al. "Brane cosmology and the self-tuning of the cosmological constant". In: *Journal of Cosmology and Astroparticle Physics* 2019.10 (Oct. 2019), p. 007. DOI: `10.1088/1475-7516/2019/10/007`. URL: `https://dx.doi.org/10.1088/1475-7516/2019/10/007`.

[48] Marc Kamionkowski and Adam G. Riess. "The Hubble Tension and Early Dark Energy". In: *Annual Review of Nuclear and Particle Science* 73.1 (2023), pp. 153–180. DOI: `10.1146/annurev-nucl-111422-024107`. eprint: `https://doi.org/10.1146/annurev-nucl-111422-024107`. URL: `https://doi.org/10.1146/annurev-nucl-111422-024107`.

[49] Planck Collaboration et al. "Planck 2018 results - V. CMB power spectra and likelihoods". In: *Astronomy & Astrophysics* 641 (2020), A5. DOI: `10.1051/0004-6361/201936386`. URL: `https://doi.org/10.1051/0004-6361/201936386`.

[50] M. Betoule et al. "Improved cosmological constraints from a joint analysis of the SDSS-II and SNLS supernova samples". In: *Astronomy & Astrophysics* 568, A22 (Aug. 2014), A22. DOI: `10.1051/0004-6361/201423413`. arXiv: `1401.4064 [astro-ph.CO]`.

[51] Julian E. Bautista et al. "Measurement of baryon acoustic oscillation correlations at z = 2.3 with SDSS DR12 Lyα-Forests". In: *Astronomy & Astrophysics* 603, A12 (June 2017), A12. DOI: `10.1051/0004-6361/201730533`. arXiv: `1702.00176 [astro-ph.CO]`.

[52] Mark S. Linton et al. "Variable sound speed in interacting dark energy models". In: *Journal of Cosmology and Astroparticle Physics* 2018.04 (Apr. 2018), p. 043. DOI: `10.1088/1475-7516/2018/04/043`. URL: `https://dx.doi.org/10.1088/1475-7516/2018/04/043`.

[53] Mark S Linton et al. "Variable sound speed in interacting dark energy models". In: *J. Cosmol. Astropart. Phys.* 2018.04 (Apr. 2018), pp. 043–043.

[54] *GNU Scientific Library Reference Manual*. 3rd. GNU Project. URL: `http://www.gnu.org/software/gsl/`.

[55] Eric Hivon et al. "MASTER of the Cosmic Microwave Background Anisotropy Power Spectrum: A Fast Method for Statistical Analysis of Large and Complex Cosmic Microwave Background Data Sets". In: *The Astrophysical Journal* 567.1 (Mar. 2002), p. 2. DOI: `10.1086/338126`. URL: `https://dx.doi.org/10.1086/338126`.

[56] J. Jewell, S. Levin, and C. H. Anderson. "Application of Monte Carlo Algorithms to the Bayesian Analysis of the Cosmic Microwave Background". In: *The Astrophysical Journal* 609.1 (July 2004), p. 1. DOI: `10.1086/383515`. URL: `https://dx.doi.org/10.1086/383515`.

[57] H. K. Eriksen et al. "Power Spectrum Estimation from High-Resolution Maps by Gibbs Sampling". In: *The Astrophysical Journal Supplement Series* 155.2 (Dec. 2004), p. 227. DOI: `10.1086/425219`. URL: `https://dx.doi.org/10.1086/425219`.

[58] Benjamin D. Wandelt, David L. Larson, and Arun Lakshminarayanan. "Global, exact cosmic microwave background data analysis using Gibbs sampling". In: *Phys. Rev. D* 70 (8 Oct. 2004), p. 083511. DOI: `10.1103/PhysRevD.70.083511`. URL: `https://link.aps.org/doi/10.1103/PhysRevD.70.083511`.

[59] M. Chu et al. "Cosmological parameter constraints as derived from the Wilkinson Microwave Anisotropy Probe data via Gibbs sampling and the Blackwell-Rao estimator". In: *Phys. Rev. D* 71 (10 May 2005), p. 103002. DOI: `10.1103/PhysRevD.71.103002`. URL: `https://link.aps.org/doi/10.1103/PhysRevD.71.103002`.

[60] D. L. Larson et al. "Estimation of Polarized Power Spectra by Gibbs Sampling". In: *The Astrophysical Journal* 656.2 (Feb. 2007), p. 653. DOI: 10.1086/509802. URL: https://dx.doi.org/10.1086/509802.

[61] C. L. Bennett et al. "NINE-YEAR WILKINSON MICROWAVE ANISOTROPY PROBE (WMAP) OBSERVATIONS: FINAL MAPS AND RESULTS". In: *The Astrophysical Journal Supplement Series* 208.2 (Sept. 2013), p. 20. DOI: 10.1088/0067-0049/208/2/20. URL: https://dx.doi.org/10.1088/0067-0049/208/2/20.

[62] M. F. Skrutskie et al. "The Two Micron All Sky Survey (2MASS)". In: *The Astronomical Journal* 131.2 (Feb. 2006), p. 1163. DOI: 10.1086/498708. URL: https://dx.doi.org/10.1086/498708.

[63] David J. Schlegel, Douglas P. Finkbeiner, and Marc Davis. "Maps of Dust Infrared Emission for Use in Estimation of Reddening and Cosmic Microwave Background Radiation Foregrounds". In: *The Astrophysical Journal* 500.2 (June 1998), p. 525. DOI: 10.1086/305772. URL: https://dx.doi.org/10.1086/305772.

[64] C. S. Kochanek et al. "The K-Band Galaxy Luminosity Function". In: *The Astrophysical Journal* 560.2 (Oct. 2001), pp. 566–579. DOI: 10.1086/322488. arXiv: astro-ph/0011456 [astro-ph].

[65] Maciej Bilicki et al. "Two Micron All Sky Survey Photometric Redshift Catalog: A Comprehensive Three-dimensional Census of the Whole Sky". In: *The Astrophysical Journal Supplement Series* 210.1, 9 (Jan. 2014), p. 9. DOI: 10.1088/0067-0049/210/1/9. eprint: 1311.5246 (astro-ph.CO).

[66] Edward L. Wright et al. "The Wide-field Infrared Survey Explorer (WISE): Mission Description and Initial On-orbit Performance". In: *The Astronomical Journal* 140.6 (Dec. 2010), pp. 1868–1881. DOI: 10.1088/0004-6256/140/6/1868. arXiv: 1008.0031 [astro-ph.IM].

[67] N. C. Hambly et al. "The SuperCOSMOS Sky Survey - I. Introduction and description". In: *Monthly Notices of the Royal Astronomical Society* 326.4 (Oct. 2001), pp. 1279–1294. DOI: 10.1111/j.1365-2966.2001.04660.x. arXiv: astro-ph/0108286 [astro-ph].

[68] O. Tange. "GNU Parallel 2018". In: (Mar. 2018). URL: https://doi.org/10.5281/zenodo.1146014.

[69] Jesús Torrado and Antony Lewis. *Cobaya: Bayesian analysis in cosmology*. Astrophysics Source Code Library, record ascl:1910.019. Oct. 2019. ascl: 1910.019.

[70] Jesús Torrado and Antony Lewis. "Cobaya: code for Bayesian analysis of hierarchical physical models". In: *Journal of Cosmology and Astroparticle Physics* 2021.05 (May 2021), p. 057. DOI: 10.1088/1475-7516/2021/05/057. URL: https://doi.org/10.1088%5C%2F1475-7516%5C%2F2021%5C%2F05%5C%2F057.

[71] George Casella and Edward I. George. "Explaining the Gibbs Sampler". In: *The American Statistician* 46.3 (1992), pp. 167–174. ISSN: 00031305. URL: http://www.jstor.org/stable/2685208 (visited on 08/07/2023).